Adaptive optics for diffraction-limited infrared imaging with 8-m telescopes

D. G. Sandler and S. Stahl

ThermoTrex Corporation, 9550 Distribution Avenue, San Diego, California 92121

J. R. P. Angel, M. Lloyd-Hart, and D. McCarthy

Steward Observatory, University of Arizona, Tucson, Arizona 85721

Received November 9, 1992; accepted February 8, 1993

When equipped with adaptive optics, the coming generation of large 6–10-m telescopes can combine huge light grasp with very sharp images. We describe a specific design concept for recovery of diffraction-limited images in the 1.6- and the 2.2-μm atmospheric windows, yielding 0.05-arcsec resolution for an 8-m telescope. Our goal has been to achieve this performance routinely by not requiring above-average atmospheric conditions or the use of unusually bright nearby stars. Atmospheric blurring is sensed with a sodium laser beacon of a few watts. Image motion is sensed by starlight, with a quadrant detector that is sensitive to the broad infrared band in which photon flux is typically largest and the field star has been sharpened by laser-beacon correction that is shared with the science target. A detailed performance analysis shows that for typical conditions Strehl ratios of >25% are expected at 2.2 μm, with the probability of finding a sufficiently bright field star exceeding 50%.

1. INTRODUCTION

We are in a period of rapid and innovative progress in adaptive optics. The technique suggested 40 years ago by Babcock[1] for sensing and correcting atmospheric blurring of starlight in real time is now being developed at several telescopes. Adaptive correction holds its greatest promise when it is used to recover diffraction-limited resolution with the new generation of telescopes with ~8-m aperture and when it is located at high-quality sites. In the next few years we should see U.S. astronomers with several such telescopes in addition to the newly completed Keck 10-m segmented-mirror telescope. The present study has as its first major goal the adaptive correction of the first of the new large telescopes with a continuous-mirror surface.

Astronomical telescopes undertake a great variety of observations. Sources under study vary over 10 orders of magnitude in brightness and are recorded at all wavelengths that are transmitted by the atmosphere. As a result, almost any adaptive correction that yields improved image sharpness can be used to the benefit of some type of observation. Relatively simple low-order systems that sense the aberrations in starlight can bring dramatic improvements to some infrared observations. Results from operational adaptive systems for astronomy have therefore been obtained almost exclusively in this area. The atmospheric windows in the infrared that are most attractive for astronomy are the H band , which extends from 1.4 to 1.8 μm in wavelength, and the K band, which extends from 2 to 2.5 μm. Array detectors for this region are approaching the high performance that has already been achieved below 1 μm with silicon CCD's, and atmospheric thermal background is not problematic, at least below 2.3 μm. Astronomers at the 3.5-m European Southern Observatory New Technology Telescope[2] and at the 3.6-m Canada–France–Hawaii Telescope[3,4] have achieved near-diffraction-limited resolution in these bands with bright reference stars. Our own program with the current 6.9-m segmented and dilute Multiple Mirror Telescope (MMT) aperture recently used phase measurements in a closed adaptive system to recover the full-diffraction-limited beam profile of a bright star, 0.075 arcsec FWHM at the 2.2-μm wavelength.[5]

The goals for military adaptive-optics systems have been more restricted and far more ambitious than for astronomy, typically consisting of optical correction of fast-moving targets observed from sites with relatively strong atmospheric blurring. To probe the detailed structure of the optical wave-front aberration, artificial starlike beacons are produced by the atmospherically scattered light of powerful laser beams that are directed toward the program object. The details of successful results with 1-m-class telescopes over the past 10 years have recently been declassified and have been reported by Fugate *et al.*,[6] Primmerman *et al.*,[7] and Sandler *et al.*[8]

We have studied by analysis and telescope experiments how laser-beacon methods could best be adapted in the near future to correct 8-m-class astronomical telescopes. These studies have led to a specific design concept based on well-established technology, to be implemented first at the 6.5-m MMT upgrade. At a later date it would be applied at the 8-m size, including the Large Binocular Telescope with twin 8.4-m apertures, which will give the highest-resolution compound adaptive system, with the resolution of a 23-m baseline.[9] The design and the calculated performance of a single 8-m system are the subjects of this paper.

Our goal for image quality is not simply a sharpening of the atmospherically blurred image but specifically to get a significant amount of optical energy into the diffraction-limited beam profile, under normal, not exceptional, at-

0740-3232/94/020925-21$06.00

mospheric conditions. We recognize that this is a difficult task, especially when the source to be corrected may be undetectable except with very long exposures. Even under the best laboratory conditions and with ideal laser interferometry, it is not easy to stabilize, to test, and to correct an 8-m mirror to better than 0.05-arcsec accuracy. Recovering such wave-front quality in the face of large and complex aberrations that change on a time scale of milliseconds is an extraordinary challenge. It requires a system that is optimized to develop and to use wave-front information to the maximum advantage. There are many potential sources of residual error that, when compounded, could defeat the high-resolution goal. The analysis and control of these errors are the main thrust of this paper. Some of the most important errors to control are those originating at the telescope itself. Here we assume that these have been reduced to the point that the inherent wave-front quality at the best sites are realized. Telescopes based on rigid honeycomb mirrors with controlled temperature, such as that being made for the MMT, are designed to meet these goals in practice.

Allowing for all sources of residual image degradation, we aim for a Strehl ratio S in the final image of $S > 0.25$ under typical conditions and $S > 0.5$ under favorable conditions. Even at 0.25, deconvolution will permit the production of images showing faint objects at the diffraction limit. The analysis given below estimates the contribution to the total mean-square wave-front error from each of the individual sources, particularly those associated with imperfect sampling of the atmospheric column to the program project by both the field-star light and the laser light.

The remainder of the paper is structured in the following manner. Section 2 gives an overview of the system design concept. Section 3 sets out the types of error that arise in the adaptive-correction system and how these combine to affect overall performance. Section 4 summarizes the optical properties of the atmosphere. We give a prescription for vertical distributions of turbulence that are believed to be representative of typical conditions at the best sites for use in the subsequent analysis. Section 5 deals with the accuracy of determining the wave-front tilt at the program object from images of a star. Contributions to the total error from the difference in light paths and from photon and detector noise, and the probability of finding field stars that are bright and close enough, are calculated. Section 6 deals with similar errors from the laser beacon, resulting from differences in the light paths (because of the finite beacon altitude) and from different noise sources. In Section 7 the overall system performance is calculated. We show that good performance in the H and the K bands is predicted, meeting the goals set out above.

2. SYSTEM OVERVIEW

A conceptual layout for the adaptive system is shown in Fig. 1. In brief, the elements are as follows:

Laser Beacon

We envisage the laser beacon to be a commercially available dye laser of a few watts of power, tuned to the sodium-resonance line.[10,11] The collimated beam of ~0.5-m diameter is directed along the line of sight by a flat in front of the telescope secondary mirror. The beacon for wave-front reconstruction is produced by resonance scattering by sodium atoms in the mesospheric layer at a 90-km altitude. The power requirement is modest because adequate sampling for wave-front correction in the infrared is provided by relatively large subaperture sizes of ~1 m, and sensing is with a CCD of high quantum efficiency and low readout noise. The aberrations caused by the finite height of the beacon are not a serious problem for correction in these infrared bands (see Section 6).

Adaptive Mirror

Our goal for lowest emissivity in the infrared is to make the secondary mirror adaptive, thus avoiding the need for pupil-reimaging optics and making adaptive correction available for all instruments, including spectrographs as well as imaging arrays. For convenience, we analyze a segmented mirror made up of 52 square segments that are controlled in piston, tip, and tilt (see Fig. 12 below). Note, however, that our system design is compatible with adaptive mirrors made from continuous flexible face sheets.

Imaging Detector

For imaging of program objects in the H and the K bands the best detector currently available is the NICMOS3 array,[12] a 256-pixel square array of HgCdTe. It has high quantum efficiency and a readout noise of 30 electrons rms. Sampling at ~0.015 arcsec/pixel would yield a field of 3.75 arcsec for one array. Because the isoplanatic fields of 15–30-arcsec diameter that are to be realized by 8-m telescopes are much larger, they will require the use of mosaics and larger individual devices.

Field-Star Motion Sensor

Atmospherically induced image motion must be corrected and is not sensed by the laser beacon.[10,11] The program

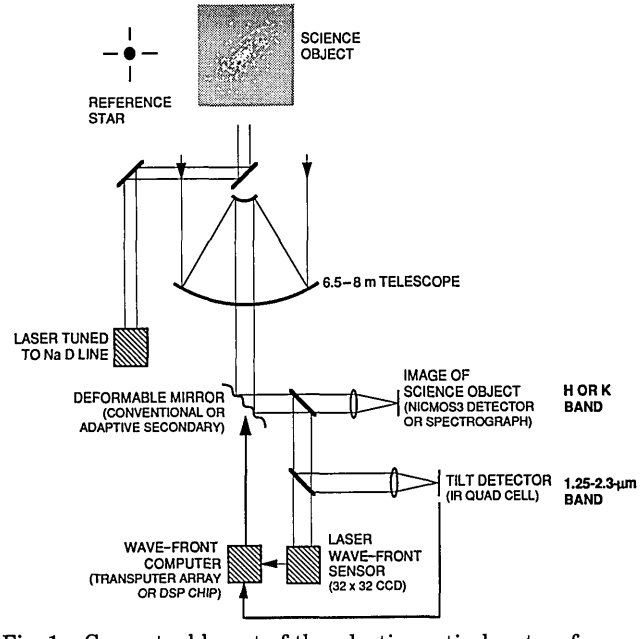

Fig. 1. Conceptual layout of the adaptive-optical system for correcting 8-m telescopes at $\lambda = 1.6$ to $\lambda = 2.2$ μm. DSP, digital signal processor. Refer to the text for an explanation of the components.

object itself may provide an adequate source, or, if it is too faint, motion must be sensed from a nearby field star.[3] Our concept calls for sensing image motion in a broad infrared band from 1.25 to 2.3 μm, where the photon fluxes are typically highest. An improvement over existing infrared detector noise is projected for a quad-cell array with the desired readout noise of 5 electrons rms. The infrared field-star images benefit from image sharpening provided by the beacon, as we show below. Under these conditions one can utilize close guide stars that at optical wavelengths would be too faint and too blurred for useful centroid measurement. In this way much fuller than usual sky cover is obtained (see Section 5).

Laser Wave-Front Sensor and Wave-Front Computer

The wave-front sensor is a Shack–Hartmann sensor,[11,13] which forms some 52 images of the laser star from different subapertures of the full pupil, with each 1-m subaperture mapping onto a 2 × 2 array of CCD pixels. Optics that allow for the alignment of each image at a pixel intersection are described by Wittman *et al.*[13] The centroid displacement of each image is proportional to the local tilt over the subaperture.

We envisage the use of a 32 × 32 pixel CCD detector of the type that is being developed by Geary,[14] which should yield readout noise as low as 3 electrons rms for a 1-ms readout time. Quantum efficiency ≥0.9 will be achieved with the thinning and the coating methods developed by Lesser *et al.*[15]

The wave-front computer will perform a 52 × 104 matrix multiply to yield the 52 piston values from the 52 x- and the 52 y-slope values. We budget 0.25 ms to perform the computation, which we project can readily be achieved with a transputer array or with one of the new commercial digital signal processor chips.

3. WAVE-FRONT ERRORS

A. Strehl-Ratio Formulas

The adaptive system that is outlined in Section 2 is used to measure and to correct for the wave-front distortion caused by turbulence between the telescope and the science object. The distortion can be pictured as a rapidly changing phase surface consisting of a global tilt, or a wedge, which causes random image motion on the science detector, in addition to random amounts of focus and astigmatism and higher modes, down to a spatial scale of ~1 m. These latter modes lead to blurring of the science image by broadening the point-spread function of the telescope. Superposed on these distortions are still higher frequency components of small amplitude, which disperse energy into the wings of the optical point-spread function but are of little consequence in the infrared. No adaptive-optics system is perfect, so there will be residual wave-front errors during operation of the system that combine to degrade the ideal Airy pattern. In this section we summarize the most important errors, which are then quantified in the remainder of the paper.

To establish notation, we assume that the wave front at point $\mathbf{x}$ at the pupil is

$$\Psi(\mathbf{x}) = \frac{2\pi}{\lambda}\boldsymbol{\Theta}\cdot\mathbf{x} + \Phi(\mathbf{x}), \tag{1}$$

where $\boldsymbol{\Theta}$ is the atmospheric wedge and $\Phi(\mathbf{x})$ is the higher-order wave-front distortion. Let the estimated tilt obtained with field-star photons be $\hat{\boldsymbol{\Theta}}$, and let the estimated higher-order wave front that is obtained with laser-star photons be $\hat{\Phi}(\mathbf{x})$. Then the instantaneous uncertainty in the value of the wedge is

$$\boldsymbol{\theta} = \boldsymbol{\Theta} - \hat{\boldsymbol{\Theta}}, \tag{2}$$

and the uncertainty in the higher-order wave front is

$$\phi(\mathbf{x}) = \Phi(\mathbf{x}) - \hat{\Phi}(\mathbf{x}). \tag{3}$$

We assume that the errors [Eqs. (2) and (3)] have zero mean, which means that the relative alignment of the science and the tilt detectors is calibrated, and we remove the overall piston of the wave front before moving the deformable-mirror actuators. The total wave-front error ψ can then be written as

$$\psi(\mathbf{x}) = \frac{2\pi}{\lambda}\boldsymbol{\theta}\cdot\mathbf{x} + \phi(\mathbf{x}). \tag{4}$$

Based on our goal of recovering diffraction-limited performance, we take the far-field Strehl ratio to be the measure of performance. To define the Strehl ratio, let $I(\mathbf{r})$ be the illumination of the detector at point $\mathbf{r}$ in the focal plane for a point-source object. The intensity in the absence of aberrations is $I_{dl}(\mathbf{r})$, the diffraction-limited Airy pattern. For an aberrated wave front the Strehl ratio is defined as[3]

$$S = \frac{\langle I(\mathbf{r}_c)\rangle}{I_{dl}(\mathbf{r}_c)}, \tag{5}$$

where $\mathbf{r}_c$ is the position of the detector pixel at the maximum of the Airy pattern and where $\langle\,\rangle$ indicates a long-exposure ensemble average over many realizations of atmospheric turbulence and measurement noise. The Strehl ratio in the presence of a wave-front error [Eq. (4)] is

$$S = \frac{16}{\pi^2 D^4}\int \exp\left[-\frac{1}{2}D_\psi(\mathbf{x},\mathbf{x}')\right] w(\mathbf{x})w(\mathbf{x}')\,d\mathbf{x}\,d\mathbf{x}', \tag{6}$$

where $w(\mathbf{x})$ is the telescope pupil function:

$$w(x) = \begin{cases} 1 & \text{if } |\mathbf{x}| < D/2 \\ 0 & \text{otherwise} \end{cases} \tag{7}$$

and where

$$D_\psi(\mathbf{x},\mathbf{x}') \equiv \langle[\psi(\mathbf{x}) - \psi(\mathbf{x}')]^2\rangle \tag{8}$$

is the structure function for the residual error ψ.

Equations (6)–(8) provide an exact expression for calculating the expected Strehl ratio [Eq. (5)] for the residual error [Eq. (4)]. However, the expression is not convenient for design analysis, since it leads to a complicated formula involving correlations of the wave-front error over the pupil. A simpler, physical model sheds more light on the effect of wave-front errors on Strehl ratio, and past experience with simulations has shown that it leads to a good approximation for the exact Strehl ratio for the conditions we treat in this paper. The simple model treats the atmospheric tilt and the high-order wave-front errors sepa-

rately. The tilt causes smearing during long exposures by causing the image to jitter about point $\mathbf{r}_c$. If we model the error in estimating the atmospheric wedge as a Gaussian random variable and assume that the main Airy envelope approximates a Gaussian profile of width λ/D, then the on-axis reduction of intensity is

$$S_\theta = \frac{1}{1 + \frac{\pi^2}{2}\left(\frac{\sigma_\theta}{\lambda/D}\right)^2}. \tag{9}$$

In Eq. (9), ${\sigma_\theta}^2$ is the mean-square tilt error:

$${\sigma_\theta}^2 = \frac{1}{2}[({\sigma_\theta}^x)^2 + ({\sigma_\theta}^y)^2], \tag{10}$$

corresponding to the average mean-square residual jitter that is measured along the axes of the infrared centroid detector. Strictly put, Eq. (9) is appropriate to cases in which the high-order errors have been partially corrected so that a significant fraction of the energy is within the first Airy disk. The rms error σ_θ contains contributions from several error sources, which we discuss below in Subsection 3.A.

The effect of high-order wave-front errors is to reduce the on-axis peak intensity by dispersing energy out of the central Airy disk. Taking ψ in Eq. (8) to be the residual high-order error ϕ, we find that

$$D_\phi(\mathbf{x}, \mathbf{x}') = 2{\sigma_\phi}^2 - 2\langle\phi(\mathbf{x})\phi(\mathbf{x}')\rangle, \tag{11}$$

where σ_ϕ is the rms error over the pupil:

$$\sigma_\phi = \left[\frac{4}{\pi D^2}\int w(\mathbf{x})\langle\phi^2(\mathbf{x})\rangle d\mathbf{x}\right]^{1/2}. \tag{12}$$

Inserting Eq. (11) into Eq. (6) with $\psi = \phi$, we find the higher-order Strehl ratio to be

$$S_\phi = \exp(-{\sigma_\phi}^2) + \frac{16}{\pi^2 D^4}\int \exp[-\langle\phi(\mathbf{x})\phi(\mathbf{x}')\rangle] \times w(\mathbf{x})w(\mathbf{x}')d\mathbf{x}d\mathbf{x}'. \tag{13}$$

We take the first term on the right-hand side of Eq. (13) as our approximation to the high-order Strehl ratio:

$$S_\phi = \exp(-{\sigma_\phi}^2). \tag{14}$$

The second term on the right-hand side of Eq. (13) represents a correction to the Strehl ratio that introduces spatial correlations of high-order wave-front errors. Equation (14), which neglects these correlations, is a good approximation for a random mix of errors totaling $\sigma_\phi \lesssim 1$ rad, which will be mostly true for our analysis. Bear in mind, however, that Eq. (14) will tend to overestimate the degradation in the Strehl ratio, since it amounts to overcounting especially the highest-frequency errors, but we consider this to be a tolerable error for our system design analysis.

Relying on our approximation that tilt and high-order errors work independently to degrade the Strehl ratio, to estimate the total system Strehl ratio S for the correction of both tilt and high-order wave-front errors we multiply the tilt and the high-order Strehl ratios:

$$S = S_\theta S_\phi. \tag{15}$$

We now proceed to describe the major contributions to σ_θ and σ_ϕ.

B. Tilt Errors

There are three major sources of error in correcting for the effects of atmospheric jitter:

1. *Anisoplanatism*

The field star that is used for tilt sensing will often be displaced in angle from the center of the science object. Thus the light from the star will encounter a slightly different atmospheric wedge than will light from the science object. Although there is a high degree of overlap between the two wedges, the small difference means that the centroid position recorded on the tilt detector of Fig. 1 will not be the true tilt. We call the rms value of off-axis sampling error ${\sigma_\theta}^{\text{iso}}$.

2. *Centroid Uncertainty*

Except for the brightest field stars, the centroid of the field star will be measured imperfectly because of photon-counting statistics in the light of the star and the sky background and because of readout noise for the infrared quadrant detector. The rms measurement uncertainty, which we call ${\sigma_\theta}^{\text{noise}}$, will depend on the size of the field-star image, the photon flux from the field star and the sky, and the properties of the detector.

3. *Temporal Decorrelation*

The atmospheric wedge will change with time, as one realization of optical turbulence evolves into another. The motion of the field-star image during integration and the time delay between measuring and correcting for the wedge will thus introduce a tilt error with the rms value ${\sigma_\theta}^{\text{time}}$.

The total one-axis mean-square tilt error is taken to be the sum of the above error sources:

$${\sigma_\theta}^2 = ({\sigma_\theta}^{\text{iso}})^2 + ({\sigma_\theta}^{\text{noise}})^2 + ({\sigma_\theta}^{\text{time}})^2, \tag{16}$$

which is used with Eq. (9) to calculate the tilt Strehl ratio S_θ.

C. High-Order Wave-Front Errors

The laser spot that is projected at 90 km will provide backscattered photons for measuring the shape of the wave front that is to be applied to the deformable mirror. There are several sources of error in this process:

1. *Cone Error for Laser Star*

The wave front from a laser star samples the turbulent layers by accumulating phase distortion along a spherical wave path with a 90-km radius of curvature. Thus the rays from the laser star sweep out a cone instead of the desired cylindrical column of air between the telescope and the science object. Because of this effect the local tilts that are measured by the Shack–Hartmann centroids do not correspond to the true atmospheric tilts but rather contain errors that accumulate linearly with the height of the turbulent layers. The result is to introduce an error into the measured wave front with the rms value ${\sigma_\phi}^{\text{cone}}$. The cone error sets the fundamental limit to

how accurately a telescope can be corrected with a single laser beacon.

2. Reconstruction Error

The Shack–Hartmann centroids contain measurement uncertainties because of photon-counting statistics and CCD noise, which depend on the number of backscattered sodium photons and hence on the laser power as well as the spot-image profiles for each subaperture. This leads to an rms error σ_{pd} in the wave-front phase-difference values that are derived from the measured slopes. These errors in turn propagate through the wave-front reconstruction process, resulting in an rms wave-front error σ_ϕ^{rec} in the final reconstructed wave front.

3. Temporal-Decorrelation Errors

Just as the atmospheric wedge decorrelates as described above, so do the wedges over each subaperture. This effect places limits on the Shack–Hartmann integration time and on the delay time between sensing the laser light and having the deformable mirror settle to the shape of the new reconstructed wave front. We call the rms error that is associated with the time delay σ_ϕ^{time}.

4. Wave-Front Fitting Error

Because of its finite number of actuators, the deformable mirror will not conform exactly to the shape of the atmospheric wave front. Also, the spatial-frequency components of turbulence with scale lengths less than the segment size will remain uncorrected. We call the resulting wave-front error the fitting error and use σ_ϕ^{fit} to denote its rms value.

5. Higher-Order Anisoplanatism

Wave-front sampling errors arise for those parts of the program object that are displaced from the axis of the laser backscatter cone. The rays from the laser star then sample a wave front that is slightly offset with respect to the wave front over the telescope. We call the rms high-order anisoplanatic error σ_ϕ^{iso}.

The total high-order wave-front error is

$$\sigma_\phi^2 = (\sigma_\phi^{cone})^2 + (\sigma_\phi^{rec})^2 + (\sigma_\phi^{time})^2 + (\sigma_\phi^{iso})^2. \quad (17)$$

Note that Eqs. (14) and (17) show that the Strehl ratio can be computed as the product of individual Strehl ratios for each error source. For example, we refer to the cone-effect Strehl ratio, which means the quantity $\exp[-(\sigma_\phi^{cone})^2]$.

4. ATMOSPHERIC CHARACTERIZATION

A. Atmospheric Parameters

To predict and to optimize the performance of any adaptive-optics system it is necessary to model the turbulence in the atmosphere, including its variation with height. Standard models for atmospheric turbulence have been developed that are appropriate for the sites used for military experiments. The sites for astronomical telescopes do not suffer from the same degree of low-altitude turbulence. In this section we describe the model atmospheres that are believed to be appropriate for the very-large-telescope sites.

We begin with a short introduction to the parameters that characterize atmospheric wave-front aberrations. These are modeled on the basis of Kolmogorov turbulence[16] as applied to the atmosphere. The validity of this description, at least in broad terms, is verified by many experiments, including our own over the 7-m aperture at the MMT.

The spatial scale of turbulent wave-front distortion at wavelength λ is characterized by a coherence length r_0, given by[17]

$$r_0^{-5/3} = 0.423k^2 \sec(\xi) \int C_n^2(z)\mathrm{d}z, \quad (18)$$

where $k = 2\pi/\lambda$ and $C_n^2(z)$ is the index-of-refraction structure constant[16] at altitude z. In Eq. (18), ξ is the zenith angle, so that $z \sec(\xi)$ is the line-of-sight distance to a turbulent layer at altitude z. The normalization is such that, over any random patch of size r_0 across the pupil, the wave-front error consists of 1 rad rms of tip–tilt plus a small (0.36-rad rms) higher-order residual error. Thus an image of a star through the patch would be diffraction limited except for image motion. For telescope diameter $D \gg r_0$, the random patches are out of phase, leading to an rms high-order wave-front distortion[18]

$$\sigma_\Phi = 0.366\left(\frac{D}{r_0}\right)^{5/6}. \quad (19)$$

The rms magnitude of the one-axis global atmospheric tilt is also a function of D/r_0:

$$\sigma_\Theta = 0.43\frac{\lambda}{D}\left(\frac{D}{r_0}\right)^{5/6}. \quad (20)$$

The parameter r_0 weights equally the turbulence at all heights in the atmosphere. However, when adaptive correction is to be made, the variations of turbulence and wind speed with height become significant factors. Suppose the wave front from one star has been perfectly corrected at a given instant, at an image of the telescope pupil. The wave front of a nearby star at angle θ follows a slightly different path through the atmosphere and will therefore not be perfectly corrected. In the limit of large D/r_0 the resulting wave-front error is given by[19]

$$\sigma_\psi^{iso} = \left(\frac{\theta}{\theta_0}\right)^{5/6} \quad (21)$$

for Kolmogorov turbulence. The size of the isoplanatic angle θ_0 is given by

$$\theta_0^{-5/3} = 2.91k^2 \sec^{8/3}(\xi) \int C_n^2(z)z^{5/3}\mathrm{d}z. \quad (22)$$

In practice Eq. (21) does not hold for the finite values of D/r_0 that are of interest here. In this case the total wave-front error is a complicated function of both θ_0 and D/r_0, and we must resort to numerical evaluation of the error. Examples are given in Section 5.

The temporal evolution of turbulence is such that, for the same star, a perfect correction at one instant will be in error at a later time Δt by an amount

$$\sigma_\psi^{time} = \left(\frac{\Delta t}{t_0}\right)^{5/6}, \quad (23)$$

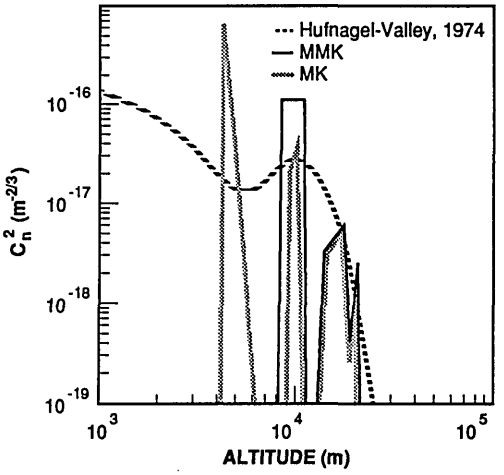

Fig. 2. Turbulent index-of-refraction profiles used in our analysis and simulations. Gray curve, MK model derived from data in Ref. 21. Solid black curve, MMK model with the 4-km MK layer moved to 10 km. Dashed curve, version of the Hufnagel–Valley model used in Ref. 23.

where

$$t_0 = 0.31\frac{r_0}{\bar{v}_w}$$

and $\bar{v}_w$ is an effective turbulence-weighted wind speed[20] for all the turbulent layers:

$$\bar{v}_w^{5/3} = \frac{\int C_n^2(z) v_w^{5/3}(z)\mathrm{d}z}{\int C_n^2(z)\mathrm{d}z}. \tag{24}$$

Equation (23) is exact only when $\bar{v}_w \Delta t$ is much less than the subaperture size. Adaptive correction must be performed on time scales $\Delta t < t_0$ to limit the degradation from rapidly changing turbulence profiles that are caused by atmospheric winds.

The turbulence power spectrum[16] obeys a $k^{-11/3}$ power law, where k is the Fourier wave number, so that in the spatial domain low-order wave-front errors are larger in magnitude than are high-spatial-frequency errors. For instance, in the Zernike representation[18] global tilt accounts for 87% of the mean-square turbulence-induced wave-front error, with focus and astigmatism accounting for the next 7%. The remaining 6% is nearly evenly distributed down to the Zernike mode whose spatial frequency corresponds to $1/r_0$. The stronger low-order modes have effectively larger isoplanatic angles and decorrelation-time constants because the correlation of two shifted but overlapping wave fronts increases as the spatial scale of the wave front grows.

We note that r_0, θ_0, and t_0 all depend on wavelength as the $\lambda^{6/5}$ power. This has serious implications for the complexity of adaptive systems. The coherence length affects system design through the number of actuators, $(\pi/4)(D/r_0)^2$, and their required stroke and also dictates guide-star brightness and laser power by defining the size of collection subapertures. The isoplanatic angle limits the use of guide stars by setting limits on the off-axis angle for a given degree of correction and on the size of the corrected image. The decorrelation time determines permissible integration times, placing a lower limit on the useful flux level for a guide star, putting strict limits on the response speed of the deformable mirror and on the required laser power, and setting the computational speed required for the wave-front processing.

B. Model Atmospheres for Good Astronomical Sites

We investigated three model turbulence profiles, shown in Fig. 2. What we call the Mauna Kea (MK) model was taken from scintillation detection and ranging (scidar) data that were obtained on Mauna Kea, as reported in Ref. 21. We supplemented the reported values of C_n^2 at a higher altitude with a strong layer at 4 km to give an r_0 of 18 cm at $\lambda = 0.5$ μm. For our calculations we assume that the 8-m telescope is located at a site 3 km above sea level. The MK model gives a value of $\theta_0 = 3$ arcsec at $\lambda = 0.5$ μm for the isoplanatic angle and is the most benign of our models in its representation of high-altitude turbulence.

The turbulence at 8–15 km plays the most important role in determining adaptive-system performance. Beland[22] recently presented C_n^2 data that were obtained from balloonborne microthermal measurements over a variety of sites worldwide at different times of the year. One feature of the data was the variability of the strength of turbulence in the 8–12-km region, where C_n^2 values ranged over almost an order of magnitude from 10^{-16} $m^{-2/3}$ to 10^{-17} $m^{-2/3}$, depending on location, jet stream conditions, and time of year. Since the MK model has a relatively thin, weak layer at 10 km, we invented a fictitious modified Mauna Kea (MMK) model, which brings the added ground layer to as high as 10 km, resulting in a stronger, thicker midaltitude layer. The MMK model gives $r_0 =$ 15 cm and $\theta_0 = 1.3$ arcsec at $\lambda = 0.5$ μm. We believe that it is pessimistic enough to set an upper bound on the deleterious effects of midaltitude turbulence on system performance under most conditions.

Finally, for comparison we also show the version of the Hufnagel–Valley (HV) family of profiles that were used in the original research of Valley and Wandzura[23] on off-axis decorrelation of Zernike modes. The HV model that is used here corresponds to $r_0 = 18$ cm and $\theta_0 = 1.5$ arcsec at $\lambda = 0.5$ μm. We show that it is midway between the MK and the MMK models in predicting the performance degradation arising from 8–15-km turbulence.

We conclude this section by summarizing in Table 1 the values of r_0, θ_0, and t_0 for the MK and the MMK models at wavelengths of 0.5, 1.6, and 2.2 μm. The assumed wind speeds were $\bar{v}_w = 25$ m/s for the MMK model and $\bar{v}_w =$ 15 m/s for the MK model. We believe that, with $r_0 = 18$ cm, relatively weak high-altitude turbulence, and relatively low wind speed, MK represents somewhat better than average conditions at a good site, whereas MMK is somewhat worse than average.

5. ANALYSIS OF TILT ERRORS

A. Off-Axis Error

A procedure for calculating the isoplanatic error in estimating low-order wave-front distortion was developed by Valley and Wandzura.[23] As shown in Appendix 1, the mean-square error for estimating tilt in one axis with an off-axis field star is

Table 1. Atmospheric Parameters for the MK and the MMK Turbulence Models at $\lambda = 0.5$, $\lambda = 1.6$, $\lambda = 2.2$ μm

Parameter	MK			MMK		
	$\lambda = 0.5$ μm	$\lambda = 1.6$ μm	$\lambda = 2.2$ μm	$\lambda = 0.5$ μm	$\lambda = 1.6$ μm	$\lambda = 2.2$ μm
r_0 (m)	0.18	0.72	1.06	0.15	0.61	0.89
θ_0 (arcsec)	3.0	12.0	17.7	1.3	5.2	7.7
t_0 (ms)	3.6	14.4	21.2	1.8	7.2	10.6

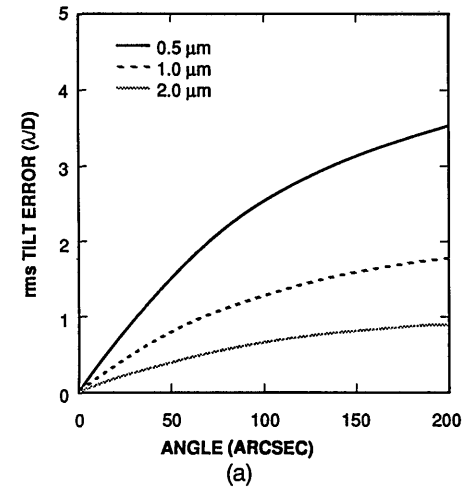

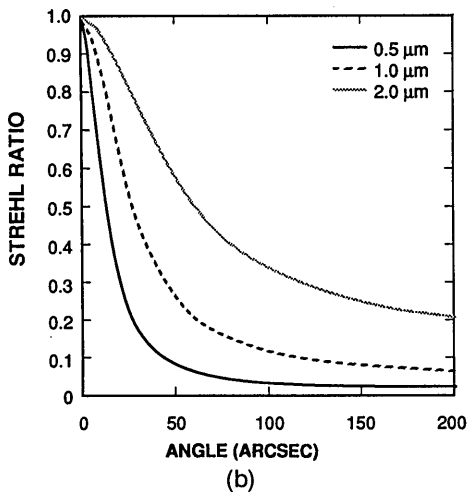

Fig. 3. Rms off-axis tilt error, and corresponding Strehl ratios versus field-star angle, for three wavelengths. The curves are for $D = 8$ m and the MK turbulence model. (a) The rms angular error (one axis) is in units of λ/D. (b) The Strehl ratios were computed with Eq. (9).

$$(\sigma_\theta{}^{\text{iso}})^2 = \frac{8}{\pi^2}(0.448)(1 - \Gamma_2)\left(\frac{D}{r_0}\right)^{5/3}\left(\frac{\lambda}{D}\right)^2, \qquad (25)$$

where Γ_2 is a correlation parameter taking on the values $\Gamma_2 = 1$ for perfect (on-axis) correlation and $\Gamma_2 = 1/2$ for no correlation between the field-star and the science-object atmospheric wedges. The correlation parameters for MK and MMK turbulence are plotted versus field-star angle in Fig. 15 of Appendix 1 below.

The rms one-axis tilt errors, obtained by averaging errors that are perpendicular and parallel to the direction of separation, for $\lambda = 0.5$ μm, $\lambda = 1$ μm, and $\lambda = 2$ μm are given in Fig. 3(a) for the MK model. Figure 3(b) shows the corresponding Strehl ratio, computed with Eq. (9). The corresponding plots for the MMK model are shown in Fig. 4. Note that since σ_θ is an angular uncertainty its absolute magnitude is independent of wavelength. [The wavelength dependence of r_0 cancels the λ^2 term in Eq. (25).] In units of λ/D, then, it exhibits a linear dependence on λ, as is shown in Figs. 3(a) and 4(a). Figure 3(b) shows that for bright stars, for which anisoplanatism is the dominant error, the permissible field separation for a tilt Strehl ratio of 0.5 is 15 arcsec in the visible and 1 arcmin at 2 μm. For the MMK model, with its strong layer at 10 km, these angles are halved, as is illustrated in Fig. 4(b).

B. Tilt-Image Centroiding Error

The tilt-image centroiding error will set magnitude limits for tilt field stars and thus determine sky coverage. We

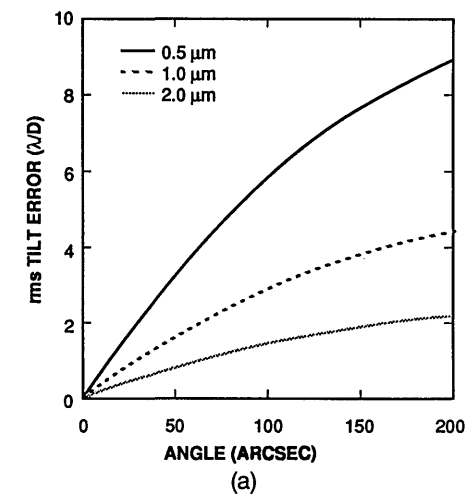

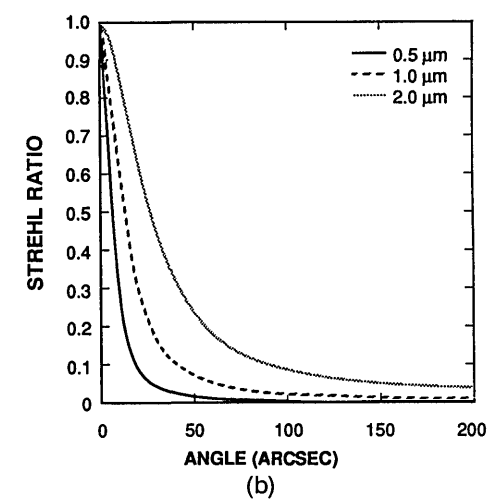

Fig. 4. Plots corresponding to those shown in Fig. 3, for the MMK turbulence model.

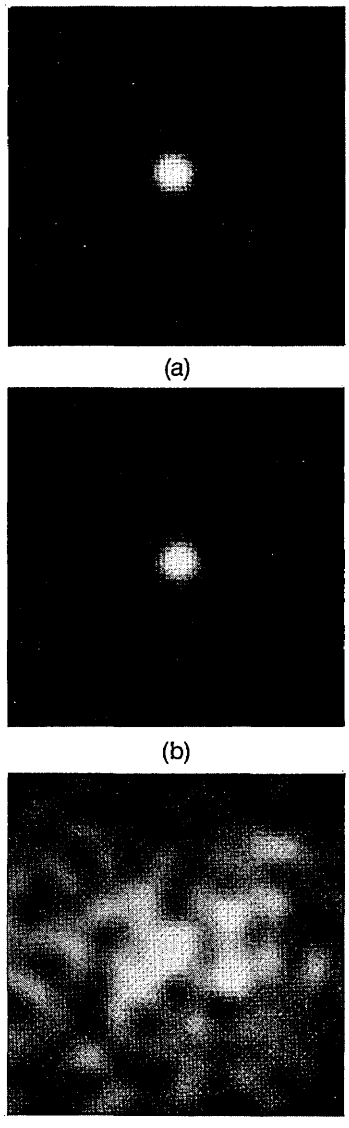

Fig. 5. Simulated images of guide stars at a 25-arcsec field angle for (a) $\lambda = 2$ μm, (b) $\lambda = 1.5$ μm, and (c) $\lambda = 0.7$ μm, obtained with the MK turbulence model. The stars were imaged through an 8-m telescope that was precorrected in the target-object direction with a sodium laser guide star.

$\sigma_\theta{}^{\text{noise}}$ is given by

$$\sigma_\theta{}^{\text{noise}} = \alpha w \frac{\lambda}{D} \frac{1}{\sqrt{N}} \left(1 + \frac{4n^2}{N}\right)^{1/2}, \tag{26}$$

show in Appendix 2 that where w is the FWHM of the image in units of the diffraction-limited image width λ/D and where the value of the parameter α that is appropriate for our situation is 0.7.

The desired values of $\sigma_\theta{}^{\text{noise}}$ are small, being limited to $\ll \lambda/D$. From Eq. (9), if the Strehl ratio from measurement error alone is to be higher than 0.6, then the rms centroid error must be less than 0.015 arcsec for H-band imaging and 0.02 arcsec for the K band.

The photon flux that is needed to produce such accurate centroiding varies as the square of the image width, in the limit of a low-noise detector. Natural images that are formed through atmospheric distortion vary in width only weakly with wavelength. However, during operation of adaptive correction with a laser pointed at the program object, image width is itself a strong function of wavelength and angular distance from the program object. It follows that there may be a strong advantage in measuring a given field-star centroid in the infrared, where the isoplanatic angle is larger and the image sharper.

In Section 6 we show that the high-order laser correction results in near-diffraction-limited correction of the science object in the H and the K bands. Thus the wave front in the object direction will be nearly flat, so that the dominant source of beam spread in the field-star direction is off-axis anisoplanatism. Figure 5 shows simulated images at three wavelengths of a field star 25 arcsec from the laser-star direction, assuming that the laser star has completely flattened the on-axis wave front. To generate the images, we performed Monte Carlo simulations with ten Kolmogorov phase screens spaced between 3 and 20 km. Rays from the field star were traced through the screens to generate the wave-front errors. The images were computed by Fraunhofer propagation of the aber-

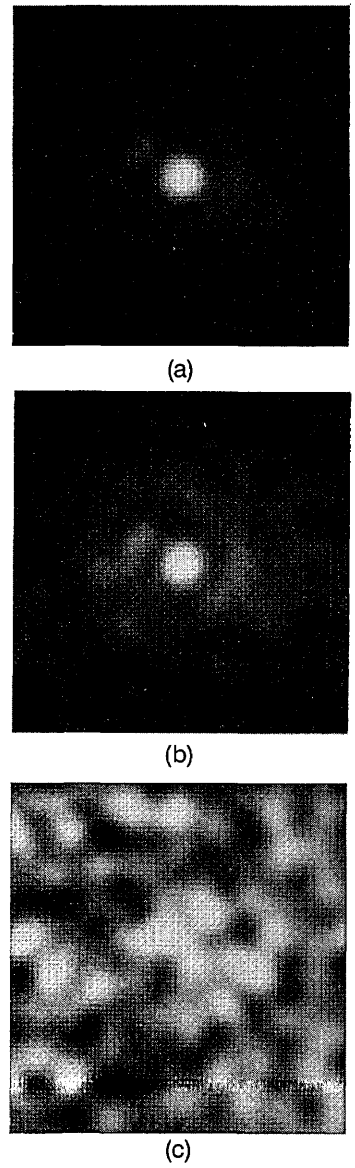

Fig. 6. Same data and conditions as for Fig. 5, obtained with the MMK turbulence model.

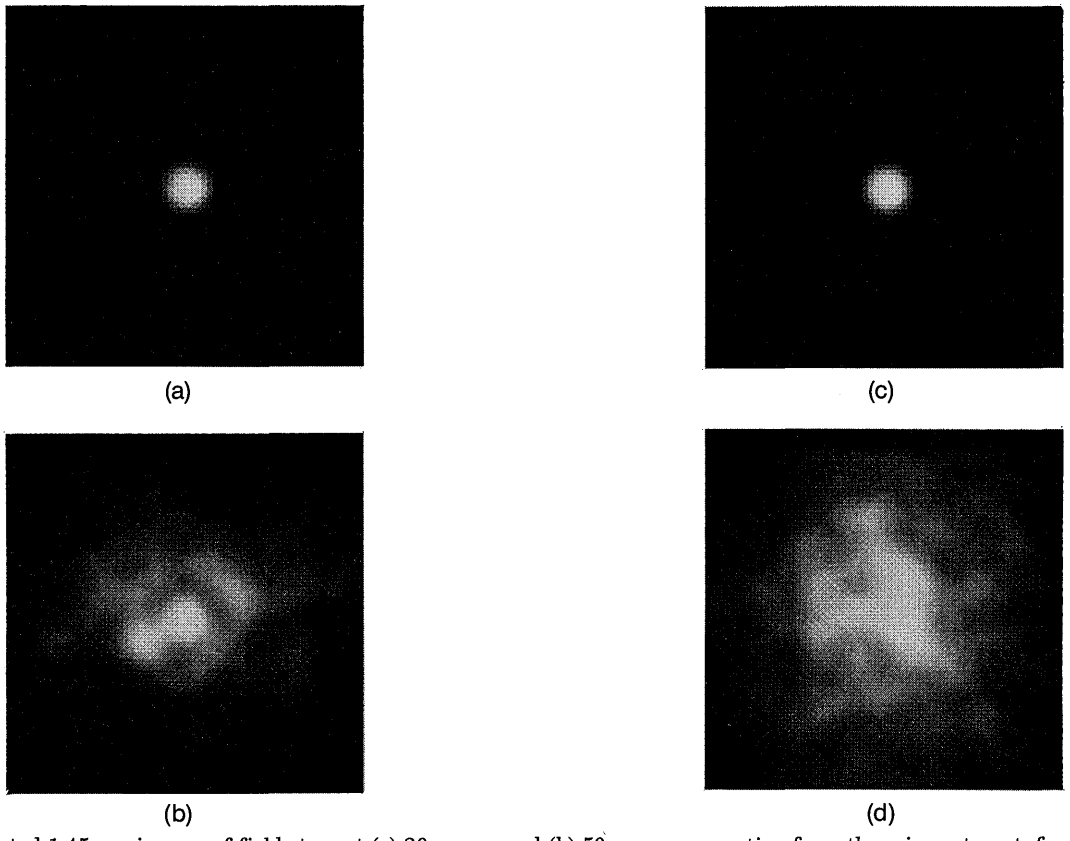

Fig. 7. Simulated 1.45-μm images of field stars at (a) 20-arcsec and (b) 50-arcsec separation from the science target, for $D = 8$ m and MK turbulence. A sodium laser beacon in the direction of the science target has been used to correct the telescope. For comparison, (c) the diffraction-limited image at 1.45 μm and (d) the uncorrected short-exposure image are also shown.

rated wave front to the far field. The wavelengths for Figs. 5(a), 5(b), and 5(c) are, respectively, 2, 1.45, and 0.7 μm, and all three correspond to MK turbulence. At 2 μm the image is diffraction limited, except for high-frequency scattered light in the wings. At 1.45 μm there is still a strong core, with the image width being 0.05 arcsec. In the red, the image is severely speckled because the laser-star wave front is completely decorrelated from the field-star wave front. Figure 6 shows the corresponding three images for MMK turbulence at a field angle of 25 arcsec. While interpreting these images we should keep in mind that even modest improvements in image width can significantly affect the tilt Strehl ratio, because of the strong dependence of the Strehl ratio on σ_θ, as given by Eq. (9).

On the basis of the estimates of image-width degradation, we assume that the field-star image centroids will be measured in a band extending from 1.25 μm, below which broadening becomes a problem, to 2.3 μm, just short of the limit at which thermal emission becomes troublesome. We calculate representative images at the wavelength 1.45 μm, near the bottom of the band. Here the diffraction-limited width is $\lambda/D = 0.0375$ arcsec.

Figure 7 corresponds to the MK model; diffraction-limited and uncorrected images are shown, along with the averages of 50 simulated short-exposure images at field-star angles of 20 and 50 arcsec. The image at $\theta =$ 20 arcsec is nearly diffraction limited wth 0.042 arcsec FWHM ($w = 1.2$); the image at $\theta = 50$ arcsec has FWHM of 0.11 arcsec ($w = 3$). Figure 8 shows the same field stars as are seen through MMK turbulence, at 10 and 25 arcsec. The image widths are, respectively, 0.042 arcsec ($w = 1.2$) and 0.12 arcsec ($w = 3.5$).

The actual image widths will be influenced by the degree of correction that is provided by the laser beacon. Monte Carlo simulations show that the effect of these residual errors is on average to increase the image widths by ~10%. In the final analysis, compared with centroiding in the visible with short-exposure image widths of 0.6 arcsec, one can achieve improvements in image widths by a factor of 5–15 for 20–30-arcsec field angles and factors of 2–6 out to 1 arcmin by combining the use of infrared field stars with a single laser star in the target direction.

The reason the infrared images remain diffraction limited at moderate field angles and retain a strong central core even out to 1 arcmin is illustrated in Fig. 9. In Fig. 9 we plot the Strehl-ratio degradation for correction of focus through second-order astigmatism as a function of field-star angle for the MK model [Fig. 9(a)] and the MMK model [Fig. 9(b)]. We generated these curves by applying the formalism described in App. 1 to Zernike modes beyond tilt. The Strehl ratios at 2 μm for these modes still exceed 0.6 out to 1 arcmin for MK and out to 25 arcsec for MMK. Similar calculations for coma and spherical aberration also indicate tolerable Strehl-ratio degradation. Thus, as one extends the laser wave-front correction to larger angles, the higher-frequency distortion (scale length 1–2 r_0) begins to decorrelate quickly, but the dominant low-order modes are still well corrected.

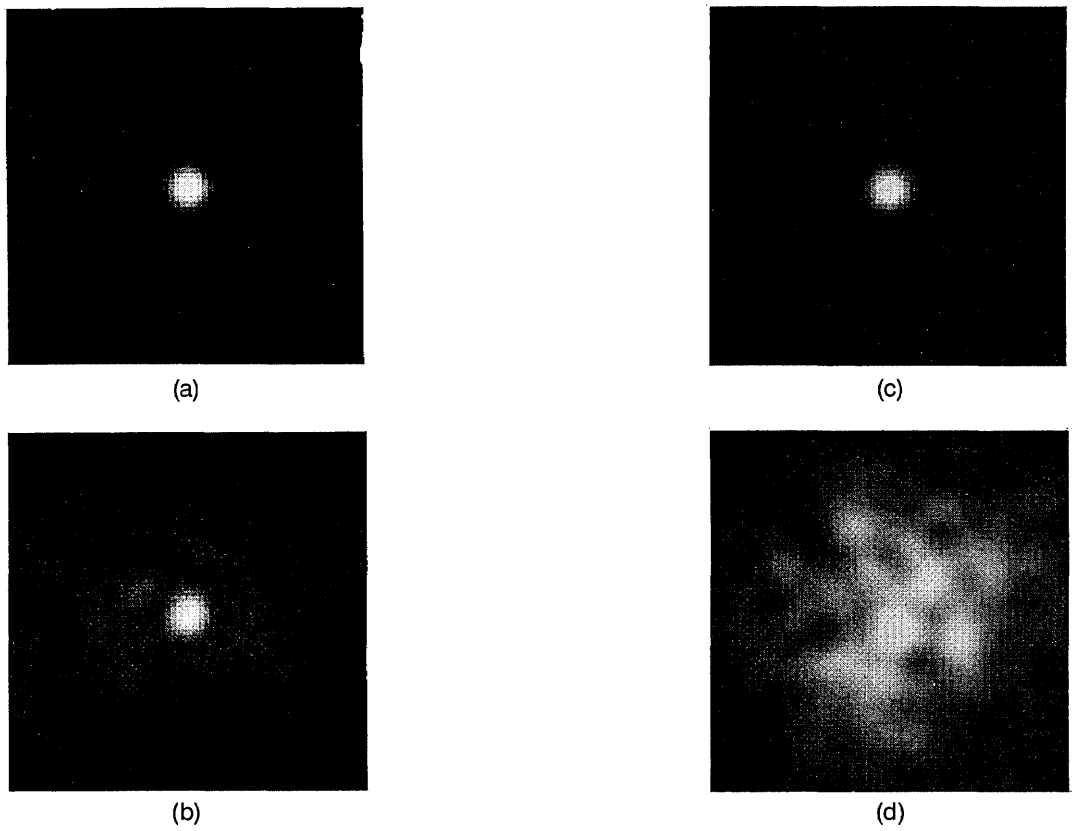

Fig. 8. Simulated 1.45-μm images of field stars at (a) 10-arcsec and (b) 25-arcsec separation from the science target, for $D = 8$ m and MMK turbulence. A sodium laser beacon in the direction of the science target has been used to correct the telescope. For comparison, (c) the diffraction-limited image at 1.45 μm and (d) the uncorrected short-exposure image are also shown.

C. Field Stars

Our goal, which is set out in Section 1, is to effect adaptive correction of faint objects without requiring unusually bright stars nearby. We now evaluate the required flux levels and the probability of finding field stars that are adequately bright and sufficiently close.

We can summarize what we have learned from the optical properties of the atmosphere as follows:

1. Wave-front tilt that is accurate enough for Strehl ratios from tilt anisoplanatism alone >0.6 at the program object is shared by field stars within a radius depending on the atmospheric model and the wave band to be corrected. From Figs. 5 and 6, we find that for model MK $r_H = 37$ arcsec and $r_K = 57$ arcsec, whereas for model MMK $r_H = 16$ arcsec and $r_H = 25$ arcsec.

2. With the laser-beacon system operating for the program object, the infrared images of field stars within these radii are partially corrected. Thus at radii of 50 arcsec (MK) and 25 arcsec (MMK) the images widths are 0.12 arcsec and reduce to 0.05 arcsec at half these radii. The appropriate wave band for field stars is 1.25–2.3 μm.

3. The temporal evolution of atmospheric turbulence sets a limit to the useful integration time for centroid measurement.[24,25] The centroid uncertainty that is due to atmospheric decorrelation has an rms value of $\sigma_\theta{}^{\text{time}}$, given by Eqs. (A11) in Appendix 1, with angular variables being replaced by time variables. Thus, when we apply Eqs. (A11) to temporal tilt decorrelation, θ_0 is replaced by t_0, and the angular variable θ becomes the time delay T between sensing and correction. To compute the tilt Strehl ratio that is due to temporal correlation, we use the average mean-square centroid error in the x and the y directions [Eq. (10)], which results in the following expression for σ_θ time:

$$\sigma_\theta{}^{\text{time}} = 0.177 \frac{T}{t_0} \left(\frac{r_0}{D} \right)^{1/6} \frac{\lambda}{D}. \tag{27}$$

Contributing to the delay T are the finite integration time of field-star photons, the detector readout time, and the control-loop response time.

4. Another property of the atmosphere is background airglow emission, which contributes to the noise in centroid measurement. From the compilation of photometric results given by Angel[26] we find that, in the chosen band for sensing field stars (H plus half each of J and K), the sky flux is ~9000 (photons/m^2)/s from a 1 arcsec × 1 arcsec area of sky. Given an 8-m telescope of total quantum efficiency $\eta = 0.4$ (optics plus detector) and square pixels of 0.15 arcsec on a side, the number of detected photo-electrons is (1833/pixel)/s.

A final parameter that is needed to complete noise estimates is the readout noise of the infrared quad cell. The best existing NICMOS3 detectors operate with a readout noise of 30 electrons rms. Readout arrays by Amber Electronics have measured noise of ≤5 electrons rms. We assume that a quad cell with an rms noise of 5 electrons will be realized in time for the 8-m telescope systems. We find

the total rms background noise n in Eq. (26) by combining in quadrature this readout noise with the sky noise, equal to $(1833T_0)^{1/2}$.

We now calculate from Eq. (27) the accuracy of centroid measurement for an infrared field star of a given photon flux or a given magnitude and image width. Since photon noise dominates, we would like to make long integrations. However, since decorrelation errors increase with time, the optimum integration time is chosen for any given star flux so as to equate the decorrelation error given by Eq. (27) and the noise error from Eq. (26). The combined error from both sources can then be expressed as an rms centroid error in seconds of arc or as the Strehl ratio from these causes alone. In Table 2 we give these errors for three star fluxes, 400, 1000 and 2500 (photons/m^2)/s in the 1.25–2.3-μm band. These fluxes correspond to H magnitudes of 18.2, 17.2, and 16.2, respectively. Two widths that are appropriate to the inner field of near-diffraction-limited resolution (0.05 arcsec) and to the edge of the useful field of shared tilt motion (0.12 arcsec) are used, and the errors for correction in each of the H and the K bands are given. We see that optimum integration times range from 4 to 16 ms and that, to keep the Strehl ratio $\geq$80% from motion measured from an image with 0.12-arcsec broadening, the flux limits are (~1600/m^2)/s (H = 16.7) for the H-band correction and (750/m^2)/s (H = 17.5) for the K band.

We note that for an infrared quad cell with n = 10 electrons rms noise the limiting fluxes increase to (2200/m^2)/s (H = 16.3) for the H band and (1100/m^2)/s (H = 17.1) for the K band. Thus sources brighter by ~0.5 H magnitude are necessary for achievement of the 0.8 Strehl-ratio goal for this higher noise level.

The limiting fluxes for infrared field stars can be compared with the corresponding fluxes that are required for centroiding with visible field stars. Since the infrared adaptive system uses 1-m subapertures and a single sodium beacon, it will provide negligible correction of the visible field-star image, even at the smallest field angles. Thus the width of the short-exposure visible quad cell image will be limited by seeing, equal to 0.5 arcsec FWHM. For an assumed quad-cell CCD with 3 electron noise, we find that fluxes of 9000 (photons/m^2)/s (K-band correction) and 17,000 (photons/m^2)/s (H-band correction) are now necessary for achievement of the 0.8 tilt Strehl-ratio goal for combined noise and temporal-decorrelation errors. Compared with the required infrared fluxes of (750/m^2)/s and (1600/m^2)/s, respectively, we see that flux limits of an order of magnitude higher are imposed for accurate centroiding with visible field stars. We also note that fluxes are typically higher in the 1.2–2.3-μm region, providing an additional advantage to using infrared field stars.

We must make an important distinction between the limiting flux levels for two modes of operation. If the program object has no stellar component, a random field star is more likely to be found toward the edge of the field of well-correlated motion, and the higher fluxes that are computed for a width of 0.12 arcsec are appropriate. However, if the program object contains a stellar component that can be at or near the laser-beacon direction, then considerably fainter fluxes will actually give a better result. For such objects there is no error from tilt anisoplanatism,

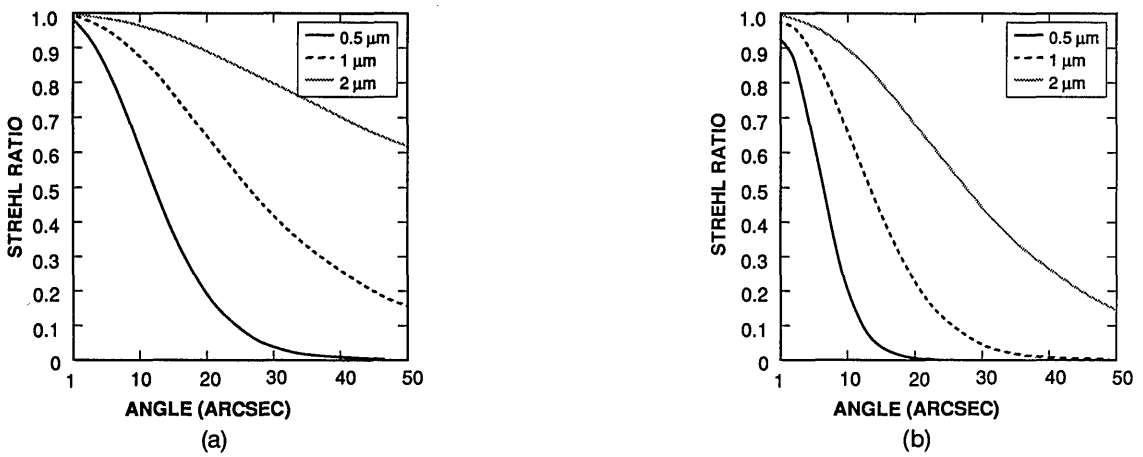

Fig. 9. Strehl ratios corresponding to the angular decorrelation of focus and astigmatism over an 8-m telescope, as a function of separation of the field star from the science target, for λ = 0.5, λ = 1, and λ = 2 μm. (a) MK turbulence, (b) MMK turbulence.

Table 2. Tilt Errors from the Combined Effects of Temporal Decorrelation and Measurement Noise[a]

Parameter	Star Flux [(photons/m^2)/s]											
	400				1000				2500			
Image width (arcsec)	0.05		0.12		0.05		0.12		0.05		0.12	
Integration time (ms)	10.0		16.1		6.6		10.8		4.4		7.4	
Rms centroid error (arcsec)	0.0103		0.0167		0.0068		0.0112		0.0046		0.0077	
Corrected wave band	H	K	H	K	H	K	H	K	H	K	H	K
Strehl ratio (%)	75	85	54	69	87	93	72	83	94	97	85	91

[a]The table gives the integration length that is necessary to balance decorrelation and measurement noise. The corresponding combined error , equal to $[(\sigma_\theta^{\text{noise}})^2 + (\sigma_\theta^{\text{time}})^2]^{1/2}$, is expressed in rms motion (arcsec), and the corresponding Strehl ratio is computed from Eq. (9) with D = 8 m. The calculation is for different star flux levels, assuming a constant background sky flux of 9000 [(photon/s)/m^2]/arcsec^2 incident at the telescope. The quad-cell pixel size is 0.15 arcsec with readout noise of 5 electrons rms, and the overall system quantum efficiency is 40%.

and the Strehl ratios given in Table 2 for an image width of 0.05 arcsec correspond to the total contribution from all sources of image-motion error. If quad-cell pixels were set at 0.05 arcsec, the flux limits become $(100/m^2)/s$ (H = 19.7) for correction of the H band and $(50/m^2)/s$ (H = 20.5) for the K band. These limits correspond to visual magnitudes of ~22, so faint that many objects of high scientific interest contain such natural reference sources. Examples are distant galaxies with active nuclei, globular clusters, and nearby galaxies.

For other small faint objects with no stellar component, such as normal galaxies at cosmological red shifts, we must evaluate the probability of finding field stars. The density of stars depends strongly on galactic latitude. For the half of the sky that is defined by bands 30° above and below the galactic plane, field stars are numerous, whereas at the galactic poles the density is 2.6 times lower. The densities of stars with the above flux values may be estimated by extrapolation to the infrared from the densities at the 0.9-μm wavelength given by Bahcall and Soniera[27] and from the model of Wainscoat *et al.*[28] At 30° latitude the density of all stars down to H magnitude 17, 18, and 19 is ~3900, ~5800, and ~8200, respectively, per square degree. At the pole the corresponding values are 1450, 2200, and 3200, respectively, per square degree. The probability of finding stars within the radii given above for the two wave bands and atmospheric models at the required flux levels may be derived from Poisson statistics, as follows.

Consider first the situation for correction of the K band. Within the 57-arcsec radius that is required in the MK model for σ_θ^{iso} corresponding to a Strehl ratio >60% from tilt anisoplanatism alone, the probability of finding at least one star brighter than the 750 $(photons/m^2)/s$ deduced above is 75% at the galactic pole and 97% at 30° latitude. For the narrower field of a 25-arcsec radius for the MMK model, the corresponding probabilities are 25% and 50%.

The probabilities are somewhat lower for finding stars to correct the H band but high enough to be of great scientific value. Again, we assume that the image width is 0.12 arcsec (conservative because the radii are smaller), and now a flux level of 1600 $(photons/m^2)/s$ is required. Under the MK-model atmosphere the probability of finding one or more stars within a 37-arcsec radius is now 33% at the pole and 65% at 30° elevation. For the MMK model the corresponding probabilities are 8% and 19%, respectively.

The above probabilities are that a field star will be found so that $(\sigma_\theta^{noise})^2 + (\sigma_\theta^{iso})^2$ alone corresponds to a Strehl ratio of 80%. It follows that, with the same probabilities, the Strehl ratio for image motion that combines all the effects of tilt anisoplanatism, photon noise from the star and the sky background, detector readout noise, and temporal decorrelation will be no worse than 48%. If brighter or nearer stars are found, the overall tilt Strehl ratio will be better.

6. HIGH-ORDER WAVE-FRONT CORRECTION

A. Cone Effect

Wave-front measurements that are made with laser stars suffer from an error source that is not present in field-star measurements. Recall from Section 3 that the wave front from a laser star samples the turbulent layers by accumulating phase distortion along a spherical wave path, with a radius of curvature H, where H is the altitude of the beacon. Consider a layer at altitude h, with distortion $\Phi(\mathbf{x})$. Instead of measuring the desired high-order phase $\Phi(\mathbf{x})$ corresponding to parallel ray paths across the projection of the pupil at h, the beacon measures $\Phi(\mathbf{x}')$, where $\mathbf{x}' = \mathbf{x}(1 - h/H)$. Thus the turbulence is sampled across an aperture of diameter $D(1 - h/H)$, and turbulence outside the cone thus generated is not measured. The rather complicated expression for the tilt-removed rms cone error, integrated over all layers, can be summarized by the formula[29]

$$\sigma_\phi^{cone} = \left(\frac{D}{d_0}\right)^{5/6}, \tag{28}$$

where the parameter d_0 scales with wavelength as $\lambda^{6/5}$. The error given in Eq. (28), sometimes called focus anisoplanatism, contains no tilt component, since the laser-star photons follow the same path up and back down through the atmospheric wedges. The parameter d_0 has a nearly linear dependence on beacon altitude, so the Strehl-ratio improvement with increasing altitude is appreciable. At λ = 0.5 μm, turbulence models used by the U.S. defense community predict that $d_0 \sim 1$ m at 15–20 km (Rayleigh backscatter) and that d_0 = 4–5 m at 90 km (resonant sodium backscatter). We have calculated d_0 at a 90-km beacon altitude for the models shown in Fig. 2, finding that $d_0 \sim 4.2$ m (MK), $d_0 = 2.7$ m (HV), and $d_0 = 2.3$ m (MMK). Just as for off-axis anisoplanatism, discussed in Section 5, the stronger turbulence at 8–12 km substantially increases the magnitude of focus anisoplanatism.

The wavelength dependence of d_0 saves the day for relatively simple laser-star infrared adaptive optics. Figure 10 shows the Strehl-ratio degradation resulting from the cone effect for an 8-m telescope as a function of wavelength. {We have extended the simple Strehl-ratio approximation [Eq. (15)] beyond its limits to show the steep drop at shorter wavelengths. The Strehl-ratio values are not strictly accurate below 0.3.} One can see from

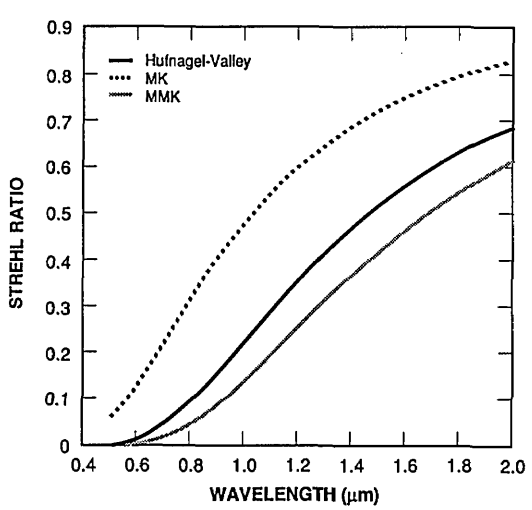

Fig. 10. Strehl ratios, resulting from finite beacon height, for the cone effect corresponding to the residual wave-front error given in Eq. (28), with D = 8 m and h = 90 km, as a function of science wavelength. Results are shown for the MK, the MMK, and the HV turbulence models.

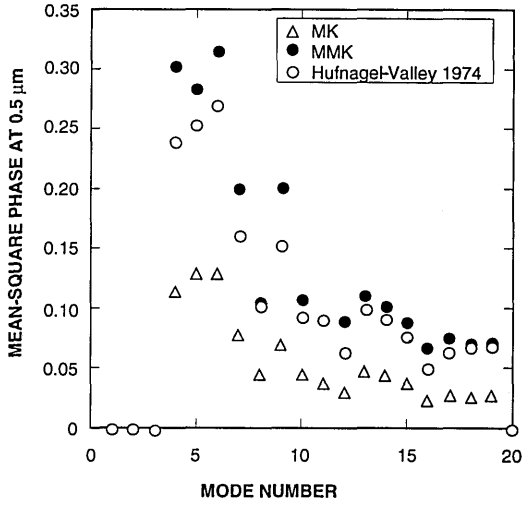

Fig. 11. Zernike decomposition of the residual cone error for $\lambda = 0.5$ μm and $D = 8$ m versus mode number. We used the mode ordering given in Ref. 18. The results for the MK, the MMK, and the HV turbulence profiles are shown.

the figure that at $\lambda = 2$ μm the Strehl ratio exceeds 0.8 for MK turbulence and 0.6 for the MMK model. At $\lambda = 1.6$ μm these values decrease to 0.76 and 0.45, respectively.

In V and R the degradation is much more severe, and one has to resort to the use of multiple Rayleigh or sodium stars,[30] possibly supplemented by field-star measurements of low-order distortion. To investigate this possibility we looked at the modal dependence of Eq. (28). Figure 11 shows the mean-square cone error at $\lambda = 0.5$ μm decomposed into Zernike components. We generated each point by averaging the results of Monte Carlo simulations, so there is some scatter in the data because of statistics. There are several points of interest. First, ~1/3 of the total phase power is in the first 10 modes, with the remaining power being broadly distributed out to the highest modes. Thus the cone effect leads to high-frequency errors that one would not hope to correct with natural stars. Second, since these errors correspond to the visible, they must be divided by 16 at $\lambda = 2$ μm, leading to small focus and astigmatism errors. Third, by inspecting Figs. 10 and 11 we see that the use of infrared field stars becomes advantageous at 1 μm, where the highest-frequency errors are tolerable and where the field star can be used to clean up the residual focus and astigmatism (modes 4, 5, 6). In the visible, however, the high-frequency errors are so large that multiple sodium stars will be needed, effectively limiting the patch below each star to $<d_0$. In this case infrared field stars may also be useful, since an analysis of multiple spot methods indicates that residual low-order errors can result from spot-position uncertainty.

B. Reconstruction Error

In our design the scattered sodium photons are used for visible Shack–Hartmann centroiding to determine the local wave-front tilts over 1-m subapertures. Different geometries have been studied in the past for arranging the subapertures with respect to the actuator points.[31] We are currently investigating new circular geometries that are appropriate for phasing an adaptive secondary. Here we analyze the case of square subapertures of width $d =$ 1 m, arranged as shown in Fig. 12, where the subaperture maps onto the quad cell that is used for centroiding. The slope measurements are used directly as tilt commands for the mirror segments. To obtain the piston commands, one converts the slope measurements to phase differences across subapertures and then integrates them with a least-squares reconstructor. In Appendix 3 we describe a simple reconstruction algorithm for determining the pistons from the phase-difference measurements and show that the reconstruction error is given by

$$(\sigma_\phi^{\text{rec}})^2 = G\sigma_{\text{pd}}^2, \tag{29}$$

where σ_{pd} is the rms phase-difference measurement noise in radians. The value of σ_{pd} depends on the laser power, the subaperture size and geometry, and the detector sensitivity.

Several different sodium lasers are being developed and are being tested by the defense and the astronomical communities. Fugate is testing a 10-W, 840-Hz laser[32] for use in hybrid sodium–Rayleigh experiments. This laser was developed by Lincoln Laboratory and uses a sum-frequency approach[33] consisting of a nonlinear combination of two YAG lines. Lawrence Livermore National Laboratory is exploring the use of a much more powerful laser with enough power for correcting down to the visible.[34] Kibblewhite's group[10] has pioneered the use of sodium lasers in astronomy, and he favors a sum-frequency approach with a laser-diode-pumped front end. Kibblewhite's initial experiments at Yerkes Observatory used a commercial cw dye laser, producing ~1 W of power. The strength of return measured by Kibblewhite for 450 mW of power was equivalent to a magnitude-12 source, integrated over a 100-nm spectral bandwidth. This corresponds to a flux of ~150 (photons/m^2)/ms, which agrees well with Fugate's data[32] of 285 (photons/m^2)/mJ.

To calculate the required laser power, we need to know how the slope measurement error σ_{pd} depends on the laser power and the imaging wavelength. Since σ_{pd} is the edge-to-edge phase-difference error in the radius, it is related to the accuracy of the measured Shack–Hartmann cen-

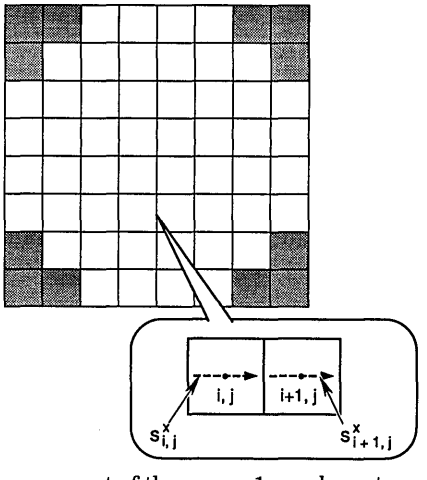

Fig. 12. Arrangement of the square 1-m subapertures that were used for our simulations of wave-front correction. There are eight subapertures across the 8-m telescope, giving a total of 52. Enlargements of adjacent subapertures ij and $i + l, j$, with the measured wave-front slopes in the x direction being indicated by the dashed lines, are also shown.

troids by

$$\sigma_{\mathrm{pd}} = 2\pi \frac{\sigma_\theta^{\mathrm{SH}}}{\lambda_0/d}\frac{\lambda_0}{\lambda}, \tag{30}$$

where $\sigma_\theta^{\mathrm{SH}}$ is the angular centroid error resulting from photon-counting statistics and readout noise [given by Eq. (26) with $D = d = 1$ m], $\lambda_0 = 0.589$ μm is the laser wavelength, and λ is the science-imaging wavelength. Combining Eqs. (26), (29), and (30), we obtain for the mean-square reconstruction error

$$(\sigma_\phi^{\mathrm{rec}})^2 = \frac{4\pi^2 G\alpha^2 w^2}{N}\left(1 + \frac{4n^2}{N}\right)\left(\frac{\lambda_0}{\lambda}\right)^2. \tag{31}$$

In Eq. (31) the number of detected photons is

$$N = 300\tau PA\eta, \tag{32}$$

where τ is the integration time (milliseconds) for laser photons, A is the area (square meters) of the subaperture, η is the total efficiency, and P is the number of watts of laser power.

To calculate the reconstruction error as a function of laser power and integration time for the $A = 1$ m^2 subapertures, we use the value $G = 0.5$ for the geometry given in Fig. 12 and the reconstruction algorithm that is described in Appendix 3. The detector is the 32×32 low-noise CCD that is discussed in Section 2, which will have quantum efficiency >0.8 at the sodium wavelength and $n = 3$ noise electrons/pixel for a 1-ms readout time. With assumed beam-train losses of 0.6, this gives a total efficiency of 0.48. The width of the laser spot, broadened during uplink through turbulence, will be 0.7 arcsec at the quadrant detectors, for a width factor $w = 6$ in Eq. (26). The appropriate value for α is 0.7. Inserting these values into Eqs. (31) and (32), we find that

$$(\sigma_\phi^{\mathrm{rec}})^2 = \frac{2.4}{P\tau}\left(1 + \frac{0.25}{P\tau}\right)\left(\frac{0.589}{\lambda}\right)^2, \tag{33}$$

where λ is the science wavelength in micrometers. For an integration time $\tau = 1$ ms, Eq. (33) yields $(\sigma_\phi^{\mathrm{rec}})^2 = 0.1$ rad^2 for $P = 3$ W at $\lambda = 1.6$ μm and for $p = 1.5$ W at $\lambda = 2.2$ μm. Thus, to keep the Strehl-ratio degradation from reconstruction errors >0.9 in both the H and the K bands, a 3-W sodium laser is required. A 4-W laser will provide a 30% margin for conditions of poorer seeing or lower atmospheric transmission.

C. Fitting Error

The wave-front fitting error describes the accuracy to which a deformable mirror can fit a Kolmogorov wave front. The error can be written as

$$\sigma_\phi^{\mathrm{fit}} = c_{\mathrm{fit}}\left(\frac{d}{r_0}\right)^{5/6}, \tag{34}$$

where d is the subaperture width and the coefficient c_{fit} depends on the type of mirror. For a segmented mirror controlled by one Shack–Hartmann centroid per segment, $c_{\mathrm{fit}} = 0.54$.[35] Thus, for the MK model, $(\sigma_\phi^{\mathrm{fit}})^2 = 0.50$ rad^2 and $(\sigma_\phi^{\mathrm{fit}})^2 = 0.26$ rad^2, respectively, for $\lambda = 1.6$ μm and $\lambda = 2.2$ μm. For the MMK model the corresponding values are 0.66 rad^2 ($\lambda = 1.6$ μm) and 0.35 rad^2 ($\lambda = 2.2$ μm).

D. Temporal-Decorrelation Errors

The temporal-decorrelation error given by Eq. (23) contains errors for all spatial frequencies of turbulence. For a small time delay, however, the contribution from global tilt decorrelation is small. To see this, consider the worst-case MMK value $\bar{V}_w = 25$ m/s and a time delay $\Delta t = 4$ ms. Then $\bar{V}_w \Delta t = 0.1$ m, which is 1/10 the subaperture width and 1/80 the full diameter of the telescope. Thus we can use Eq. (23) to estimate $\sigma_\phi^{\mathrm{time}}$.

For the delay time we take a total of $\Delta t = 3$ ms for measuring and correcting the high-order wave front. We use 1 ms to integrate photons from the laser beacon, as discussed above in Subsection 6.B. Another 1 ms is used to read out the Shack–Hartmann CCD. The remaining 1 ms is divided among wave-front reconstruction (200 μs), interface communication (400 μs), and deformable-mirror response (400 μs). With this timing budget we find that $(\sigma_\phi^{\mathrm{time}})^2 = 0.038$ rad^2 for MK turbulence at $\lambda = 2.2$ μm, increasing to 0.073 rad^2 at $\lambda = 1.6$ μm. For MMK turbulence the values are $(\sigma_\phi^{\mathrm{time}})^2 = 0.12$ rad^2 ($\lambda = 2.2$ μm) and $(\sigma_\phi^{\mathrm{time}})^2 = 0.23$ rad^2 ($\lambda = 16$ μm).

E. High-Order Anisoplanatism

Equation (21) gives the total wave-front error that arises from using a beacon at angular separation θ from the science object. In Section 4 we calculated the contributions to $\sigma_\psi^{\mathrm{iso}}$ corresponding to tilt, focus, and astigmatism errors and found that even for $\theta \gg \theta_0$ these low-frequency modes remain partially corrected. Whereas there will be high-frequency contributions to $\sigma_\phi^{\mathrm{iso}}$ for field-star wave-front sensing as θ approaches or exceeds θ_0, the predominant source of anisoplanatism for laser beacons arises from pointing and tracking the beacon. These errors can place modest demands on the tracking system for defense applications involving slewing the beacon ahead of the target. For infrared astronomy, however, the demands are much less stringent. Consider, for example, the worst case given in Table 1, namely, $\theta_0 = 5.2$ arcsec for the MMK model at $\lambda = 1.6$ μm. As long as the pointing of the beacon is accurate to within 1 arcsec of the science object, from Eq. (21) we find that $(\sigma_\phi^{\mathrm{iso}})^2 \le 0.05$ rad^2. The requirement becomes even more modest at longer wavelengths and for MK turbulence, so we will consider this error negligible.

F. Summary of High-Order Wave-Front Errors

Table 3 summarizes the high-order wave-front errors that are derived in this section. Each error source is listed

Table 3. Error Sources for Correcting the High-Order Wave-Front across an 8-m Telescope at $\lambda = 1.6$ μm and $\lambda = 2.2$ μm[a]

Parameter	MK		MMK	
	$\lambda = 1.6$ μm	$\lambda = 2.2$ μm	$\lambda = 1.6$ μm	$\lambda = 2.2$ μm
$(\sigma_\phi^{\mathrm{cone}})^2$	0.28	0.15	0.77	0.41
$(\sigma_\phi^{\mathrm{rec}})^2$	0.10	0.10	0.10	0.10
$(\sigma_\phi^{\mathrm{time}})^2$	0.073	0.038	0.23	0.12
$(\sigma_\phi^{\mathrm{fit}})^2$	0.50	0.26	0.66	0.35
σ_ϕ^2	0.95	0.55	1.76	0.98
S_ϕ	0.39	0.58	0.17	0.37

[a]The value of $\sigma_\phi^{\mathrm{rec}}$ assumes a 1.5-W sodium laser for $\lambda = 2.2$ μm and a 3-W laser for $\lambda = 1.6$ μm.

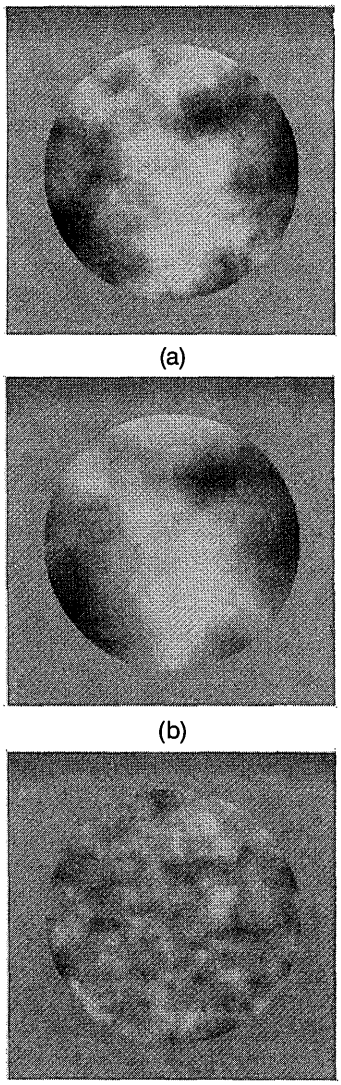

Fig. 13. Contours of phase distortion corresponding to a Monte Carlo simulation of wave-front correction for $D = 8$ m and $\lambda = 2$ μm. (a) Kolmogorov distortion across the telescope (0.4 wave rms) before adaptive correction. (b) The reconstructed wave-front corresponding to tilt and piston phasing of 1-m subapertures. (c) The residual wave-front error after correction (0.11 wave rms), obtained by differencing (a) and (b).

along with its value for MK and MMK turbulence. For each turbulence model the errors are tabulated separately for $\lambda = 1.6$ μm and $\lambda = 2.2$ μm. Also listed for each case are the total high-order error $\sigma_\phi{}^2$ and the corresponding Strehl ratio.

We performed Monte Carlo simulations of high-order wave-front reconstruction with a laser beacon at 90 km. We generated the wave front that was accumulated by light from the beacon by integrating over ten Kolmogorov phase screens, and we constructed slope measurements for the subapertures that are shown in Fig. 12. Measurement noise of magnitude σ_{pd} was added to the slope values, and an iterative algorithm [Eqs. (A20)–(A23) below] was used to reconstruct the wave front. We modeled the effect of temporal decorrelation by shifting the reconstructed wave front by an amount $v_w \Delta t$. A sample reconstruction is pictured in Fig. 13. Figure 13(a) is a gray-scale contour plot of the phase at $\lambda = 2.2$ μm over the 8-m pupil, for a realization of MK turbulence. The rms value is $\sigma_\Phi = 2.5$ rad. Figure 13(b) shows the reconstructed phase contour, and Fig. 13(c) is the residual error corresponding to the difference between Figs. 13(a) and 13(b). The residual rms error for this realization is 0.7 rad, which agrees well with the ensemble average value $\sigma_\phi = 0.74$ rad that is given in Table 3. Figure 14 shows the same phase profiles displayed as three-dimensional plots. From Figs. 13(c) and 14(c) we can see that the residual error consists mostly of high frequencies, with the exception being near the edges of the aperture, where the cone-effect errors are largest.

7. TOTAL SYSTEM PERFORMANCE AND CONCLUSIONS

Bringing together the results of Sections 5 and 6, we show in Table 4 the overall performance, combining the effects of tilt and high-order errors by multiplication of Strehl ratios (Section 3). The values of S_ϕ are taken from Table 3. Two values of S_θ are shown for each wave band. As discussed in Section 5, $S_\theta = 0.48$ is appropriate for the combined errors of tilt anisoplanatism and noise when a random field star must be used, and the corresponding probabilities of finding stars that are bright enough for this accuracy are tabulated. $S_\theta = 0.8$ is appropriate when the corrected field can be centered on a star in the program object and there is no error from tilt anisoplanatism. A Strehl ratio of 0.8 corresponds to a faint centered star with $H = 19.7$ (for correction in the H band) or $H = 20.5$ for the K band.

The projected values for the overall Strehl ratio give the image quality that is expected at the center of the field defined by the direction of the laser beacon. For the MK model these values meet our desired goal of $S \geq 0.25$ for the K band. The H-band performance exceeds our goal for the case of a program object tilt star. The H-band value $S = 0.20$ for a random tilt star falls short of our goal, but only marginally. Under the poorer conditions of the MMK model, the H-band Strehl ratios decrease to 9–14%, but the K-band images still come close to or exceed the goal. We conclude that H-band observations are best undertaken when high-altitude turbulence is at the MK level or better. Not only is the Strehl ratio good, but the probability of finding guide stars is high. Under the poorer conditions of the MMK model, K-band observations still remain possible.

To investigate the sensitivity of predicted performance to varying atmospheric conditions, consider the situation in which the value of $C_n{}^2$ is multiplied at every altitude by a constant. For instance, multiplying $C_n{}^2$ by 0.65 results in a 30% increase in the values of r_0, θ_0, d_0, and t_0, as might be expected during periods of better seeing. Conversely, multiplying $C_n{}^2$ by 1.95 results in a 30% decrease in these parameters, encountered during periods of worse seeing or during correction far off zenith. Under such conditions the cone, the time-delay, and the fitting errors in Table 3 are multiplied by the same factor that is multiplying $C_n{}^2$, either 0.65 or 1.95. The reconstruction error varies as $r_0{}^{-2}$, so this error is multiplied by either 0.45 (30% better seeing) or 1.69 (30% worse seeing). The net effect of these variations is to change the MK high-order Strehl ratio to 71% on the upper end and to 35% on the

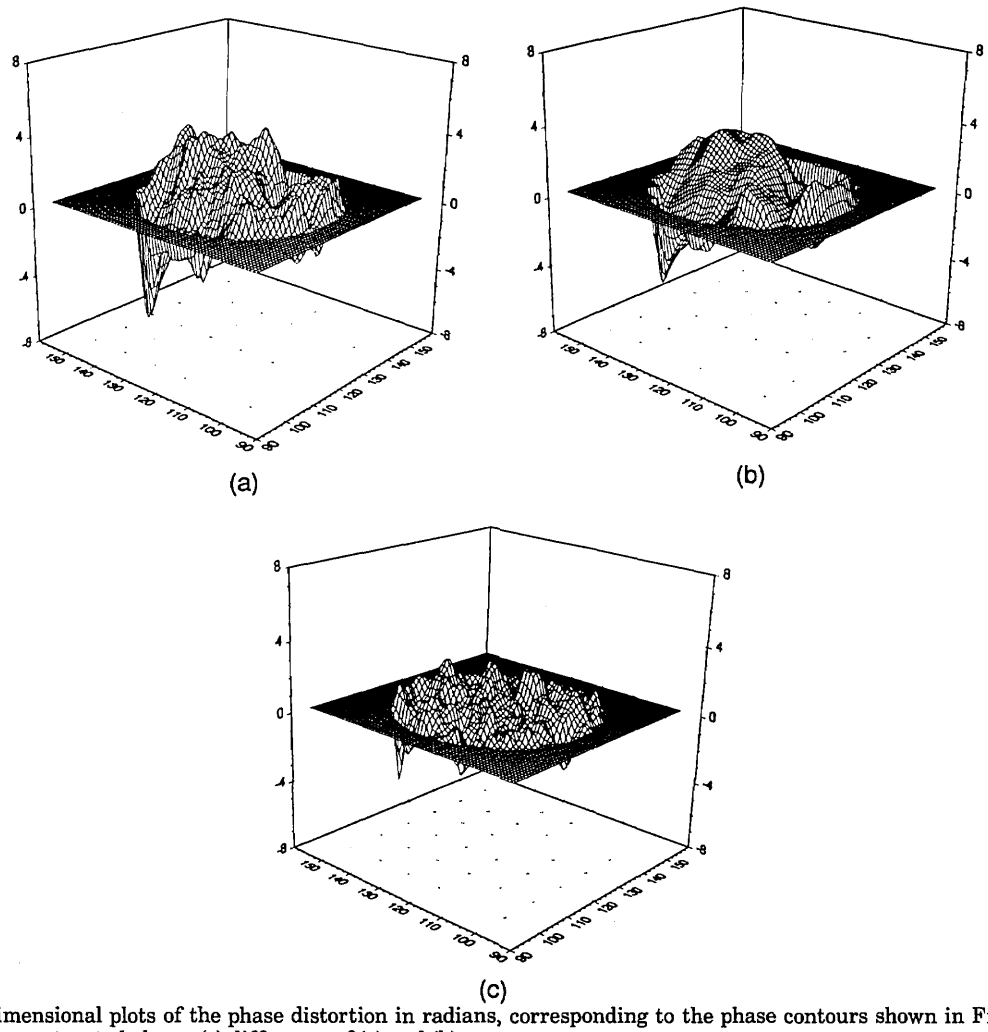

Fig. 14. Three-dimensional plots of the phase distortion in radians, corresponding to the phase contours shown in Fig. 13. (a) Uncorrected phase; (b) reconstructed phase; (c) difference of (a) and (b).

Table 4. Contributions to the Total Strehl Ratio for the *H* ($\lambda = 1.6$ μm) and the *K* ($\lambda = 2.2$ μm) Wave Bands[a]

Parameter	MK				MMK			
	$\lambda = 1.6$ μm		$\lambda = 2.2$ μm		$\lambda = 1.6$ μm		$\lambda = 2.2$ μm	
S_ϕ	0.39		0.58		0.17		0.37	
S_θ	0.5	0.8	0.5	0.8	0.5	0.8	0.5	0.8
S	0.20	0.31	0.29	0.46	0.09	0.14	0.19	0.30
P_{pole}	33%		75%		8%		25%	
$P_{30°}$	65%		97%		19%		50%	

[a]The high-order Strehl ratios S_ϕ are taken from Table 3. The tilt Strehl ratios S_θ are appropriate if one is using a field star (50%) or a faint star that is coincident with the laser beacon (80%) as analyzed in Section 5. The total Strehl ratios are given by $S = S_\theta S_\phi$. The probabilities for finding at least one sufficiently bright field star within the required angle to give a 50% tilt Strehl ratio are given for the galactic pole (P_{pole}) and for 30° galactic latitude ($P_{30°}$).

lower end, for $\lambda = 2.2$ μm. For $\lambda = 1.6$ μm, the 48% Strehl ratio in Table 3 changes to 55% for better conditions and to 16% for worse conditions. For the MMK model the higher (lower) Strehl ratios are 54% (15%) for $\lambda = 2.2$ μm and 33% (3%) for $\lambda = 1.6$ μm.

Under the same transformations of C_n^2 the values of S_θ in Table 4 also change, from 50% to 61% (34%) for random field stars and from 80% to 85% (66%) for field stars that are coincident with the laser beacon. Combining these variations with those given above for the high-order Strehl ratios, we find that for the MK model the total Strehl ratios for a random field star range from 43% for better conditions to 12% for worse conditions, at $\lambda = 2.2$ μm, compared with 29% for the unperturbed MK C_n^2 profile. For the MMK model at $\lambda = 2.2$ μm, the Strehl ratios range from 33% to 5% around the unperturbed mean of 19%. Similar variations in the expected Strehl ratio occur for $\lambda = 1.6$ μm and for the cases that use a faint star within the program object. We conclude that approximately ±50% variation in the Strehl ratio occurs for 30% variations in the seeing, assuming that the changes in the strength of turbulence occur evenly for all layers.

It is worth noting the Strehl ratio alone does not tell the whole story. Residual high-order wave-front errors spread energy from the diffraction peak into a profile that is much more centrally peaked than is the original atmospheric blur. The profiles of images with $\sigma_\phi > 1$ will not be unlike those outside the isoplanatic angle that are shown in Fig. 8. The effect of errors in image motion are even more benign. This can be seen from Table 2, in which in the worst case of guiding by a field star at 160 (photons/m^2)/s the motion is only 0.018 arcsec rms, and thus the broadening does no more than increase the image width by a factor of 1.4 to 0.070 arcsec. The fraction of energy within this width is given by S_ϕ, not by the lower combined Strehl ratio.

The scientific potential for a system that performs at the levels at which we calculate is immense, as we discuss below. We are encouraged because the proposed system is relatively simple and because it uses components that are at, but not beyond, the state of the art. One laser suffices, whose power requirements of 3–4 W are readily achieved. We call for a high-performance CCD for the Shack–Hartmann sensor, and such devices are currently being tested. The infrared broadband quad-cell tector, critical for access to the faintest close guide stars, calls for 5 electrons rms readout noise, already proven in readout arrays. Our preference for adaptive correction at the secondary mirror will require a significant advance, but the projections in this paper do not depend on it. More conventional relay optics and adaptive mirrors can be used.

Based on these calculations and on current experience with the segmented MMT, we plan to implement the system for the new 6.5-m mirror. Depending on experience with this first implementation, there are two possible improvements while staying within the limitation of a single laser. The first of these is to upgrade the beacon system and the adaptive-mirror hardware. We could improve the *H*-band performance under the poor conditions of the MMK atmosphere by halving the size of the subapertures to 0.5 m and by halving the laser integration time. In this way the temporal and the decorrelation errors could both be reduced to 0.1 rad^2. The overall Strehl ratio at *H* would then be increased to 30% for even the worst case of Table 4. The price is an eightfold increase in laser power, to 16–32 W, and a quadrupling of the number of subapertures to 208. This upgrade represents a significant increase in cost and complexity and is probably best delayed until the conditions at a given site are well understood. It is hoped that conditions as bad as those of the MMK model will be infrequent. On the other hand, we may find that with such improvements and under good conditions diffraction-limited imaging in the *J* band centered at 1.25 μm becomes attractive.

A second improvement is possible if low-altitude topographic turbulence is weak at the site and if the telescope and the enclosure do not add appreciably to the high-frequency wave-front distortion. Under these conditions our assumption that correction is made at an image of the telescope entrance pupil is not optimum. Correction that is made at a pupil corresponding to the mean height of turbulence could easily result in an increase in the isoplanatic angle by a factor of 2. Furthermore, if the high-altitude turbulence is dominant, the wave front that is measured by the Shack–Hartmann sensor can be applied at increased scale to the adaptive mirror, thus avoiding some of the cone-effect error. These changes would result in a substantial increase in the Strehl ratio, the isoplanatic field, and the probability of finding guide stars. For this reason it is most important to control the mirror and local seeing in large telescopes if adaptive optics is to reach its limits.

In principle, turbulence at different levels can be distinguished and measured through the use of multiple beacons and triangulation. Such methods would further help in the infrared and will be necessary for the production of widely applicable systems for optical correction. However, they will involve a large increase in complexity in what is already difficult and should probably await further experimentation and optimization on smaller telescopes.

The results of this study show that adaptive optics is likely to have a profound effect on the use of an 8-m class telescope in the infrared. Given that diffraction-limited resolution can be achieved with the aid of faint and common stars, adaptive correction could become the rule rather than the exception. The combination of huge light grasp and sharp images provided by a large telescope working at its diffraction limit is an enormous advantage. The isoplanatic angle, which is independent of telescope size, is highly resolved by big telescopes. Thus fields of at least 20-arcsec diameter imaged with 0.05-arcsec resolution contain 160,000 spatial-resolution elements.

The resolution of the Hubble Telescope after it is fitted with correcting optics will also be ~0.05 arcsec. By combining data, researchers will produce maps of uniformly high resolution over nearly a decade of wavelength. Later the Hubble is to be fitted with its own infrared instrument, NICMOS. Its imaging resolution will be 3–4 times poorer and its light-gathering power an order of magnitude less, but it will have the advantage of a well-calibrated and a uniform response, with no limitation on field angle and much darker sky in the absence of airglow, which is up to 100 times the natural background. We see that the ground-based telescope's strength will be in spectroscopy and detailed imaging, whereas the Hubble's strength will be in accurate photometric measurements, especially of diffuse and faint objects such as highly redshifted galaxies.

APPENDIX 1: ANISOPLANATISM IN ESTIMATING ZERNIKE COEFFICIENTS WITH OFF-AXIS FIELD STARS

The use of an off-axis field star to determine phase correction introduces an isoplanatic error in the phase determination. The error depends on the degree to which the phase fluctuations over the two paths are decorrelated. Let Ψ denote the object wave front and $\hat{\Psi}$ the phase estimate as determined from the reference source. Then the mean-square error is

$$(\sigma_\Psi{}^{\text{iso}})^2 = \frac{4}{\pi D^2}\int w(\mathbf{x})\langle[\Psi(\mathbf{x}) - \hat{\Psi}(\mathbf{x})]^2\rangle d\mathbf{x}, \tag{A1}$$

which may be written as

$$(\sigma_\Psi{}^{\text{iso}})^2 = 2(1 - \Gamma)\sigma_\Psi{}^2, \tag{A2}$$

where Γ is the normalized covariance of the phase:

$$\Gamma = \frac{4}{\pi D^2 \sigma_\Psi{}^2} \int w(\mathbf{x}) \langle \Psi(\mathbf{x}) \hat{\Psi}(\mathbf{x}) \rangle d\mathbf{x}. \tag{A3}$$

We wish to estimate off-axis errors in Zernike coefficients. Thus we decompose both target and off-axis wave fronts into Zernike modes:

$$\Psi(\mathbf{r}) = \sum a_n Z_n(\mathbf{r}), \tag{A4}$$

$$\hat{\Psi}(\mathbf{r}) = \sum b_n Z_n(\mathbf{r}). \tag{A5}$$

If we define $\Gamma_n = \langle a_n b_n \rangle / \langle a_n{}^2 \rangle$, then the quantity

$$\Delta_n = 2(1 - \Gamma_n) \langle a_n{}^2 \rangle \tag{A6}$$

represents the error that is due to correcting a given Zernike mode with the sampled coefficients b_n rather than with the true coefficients a_n. Given a model for the atmospheric index-of-refraction structure constant $C_n{}^2$, the normalized correlation for a given Zernike mode may be evaluated as

$$\Gamma_n(\theta) = \frac{\int \gamma_n(z\theta) C_n{}^2(z) dz}{\int C_n{}^2(z) dz}, \tag{A7}$$

where the integration is carried out over altitude z and where γ_n is the normalized correlation function for a single turbulence layer at altitude z. The function γ_n may be expressed as

$$\gamma_n(z\theta) = \frac{C_{jm}{}^{jm}(\Delta) \pm C_{j-m}{}^{jm}(\Delta)}{C_{jm}{}^{jm}(0)}, \tag{A8}$$

where $\Delta = z\theta/D$. The + is appropriate for terms of even parity, the − for terms of odd parity; m is the azimuthal order of the Zernike mode, and $2j + m$ is the radial order. The quantity $C_{j'm'}{}^{jm}(\Delta)$ is given by

$$\begin{aligned} C_{j'm'}{}^{jm}(\Delta) = (-)^{j+j'} 8\pi^2 C R^\beta \varepsilon(m, m') [(2j + |m| + 1) \\ \times (2j' + |m'| + 1)]^{1/2} \int_0^\infty dz z^{-\beta-3} J_{|m-m'|}(2z\Delta) \\ \times J_{2j+|m|+1}(z) J_{2j'+|m'|+1}(z), \end{aligned} \tag{A9}$$

where, for $m > m'$ and m, m' positive, $\varepsilon(m, m') = 1$ and $\varepsilon(m, -m') = (-1)^{m'}$.

For a layer of Kolmogorov atmospheric turbulence of thickness δ and structure constant $C_n{}^2$, $\beta = 5/3$ and $C = 0.207 k^2 C_n{}^2 \delta$. Closed-form expressions for $\Delta > 1$ and $\Delta = 0$ are given in Ref. 23; a closed-form expression for $0 \le \Delta \le 1$ is found in Ref. 36.

We now apply Eqs. (A6)–(A9) to the Zernike tilt modes. A point of distinction is in order between centroid tilt, which is related to the average slope of the wave front, and Zernike tilt, which corresponds to the best-fit plane over the pupil. Strictly speaking, since we are interested in centroid tilt, our analysis should be applied to off-axis errors in this quantity. However, because the two types of tilt have very similar variances (~10% discrepancy) and since the formalism we use below has already been presented in Ref. 20 for Zernike tilt, we choose to analyze the off-axis error in estimating Zernike tilt.

The longitudinal tilt error (along the x axis joining the science object and the field star) has a different correlation coefficient than does the lateral tilt (along the y axis, perpendicular to the field-star direction). For the longitudinal tilt, we have from Eq. (A6)

$$\Delta_2 = 2(0.448)(1 - \Gamma_2) \left(\frac{D}{r_0} \right)^{5/3}, \tag{A10}$$

where the factor $(0.448)(D/r_0)^{5/3}$ is the uncorrected one-axis mean-square tilt for a Kolmogorov phase spectrum.[18] Equation (25) in Section 5 for $\sigma_\theta{}^{\text{iso}}$ follows from Eq. (A10).

It is useful to have working formulas for the angular isoplanatic errors in the longitudinal and the lateral directions, which we denote by $\sigma_\theta{}^x$ and $\sigma_\theta{}^y$, respectively. By expanding Eq. (A10) and using Eqs. (A7)–(A9), we derive the following expressions:

$$\frac{(\sigma_\theta{}^x)^2}{(\lambda/D)^2} = 0.0472 \left(\frac{\theta}{\theta_0} \right)^2 \left(\frac{D}{r_0} \right)^{-1/3} - 0.0107 \left(\frac{\theta}{\theta_0} \right)^4 \left(\frac{D}{r_0} \right)^{-7/3}, \tag{A11a}$$

$$\frac{(\sigma_\theta{}^y)^2}{(\lambda/D)^2} = 0.0157 \left(\frac{\theta}{\theta_0} \right)^2 \left(\frac{D}{r_0} \right)^{-1/3} - 0.00214 \left(\frac{\theta}{\theta_0} \right)^4 \left(\frac{D}{r_0} \right)^{-7/3}. \tag{A11b}$$

The leading terms in Eqs. (A11), quadratic in θ, are valid out to field angles $\theta \le 0.5(D/r_0)\theta_0$; the sum of the quadratic and the fourth-order terms is accurate out to $\theta \le (D/r_0)\theta_0$. For large angular separation the tilt correlation Γ_2 approaches 1/2, so that the total expected tilt contribution to the phase error approaches the uncorrected value. We note here that no *a priori* knowledge of $C_n{}^2$ is assumed, so that an optimal estimation of a given Zernike coefficient is not made. Hence the variance of the error that is due simply to using the measured off-axis coefficients may exceed the error in the absence of correction. If the measurement of the coefficients is supplemented by a knowledge of $C_n{}^2$, then an optimal estimate can be made, substantially reducing the error at large field angles. In this paper we have restricted ourselves to consideration of the isoplanatic error without optimal estimation.

Correlation functions for two different models of turbulence for various modes are illustrated in Fig. 15. The horizontal axis is appropriate for an 8-m-diameter telescope. The correlation functions for the MMK model [Fig. 15(b)] fall off more rapidly than do those for the MK model [Fig. 15(a)] because of the strong 10-km layer. In fact, since most of the turbulence in the MMK model is located in one layer at 10 km, the integrated correlation functions are approximately the correlations for a single layer.

APPENDIX 2: CENTROIDING ERROR

In this appendix we estimate tilt errors that are due to centroiding uncertainty that is introduced by photon counting and detector noise. Tyler and Fried[37] determined the theoretical limit to the angular resolution of a quadrant detector in terms of the optical transfer function of the system and the object irradiance. The expression for the angular measurement error with a point source is

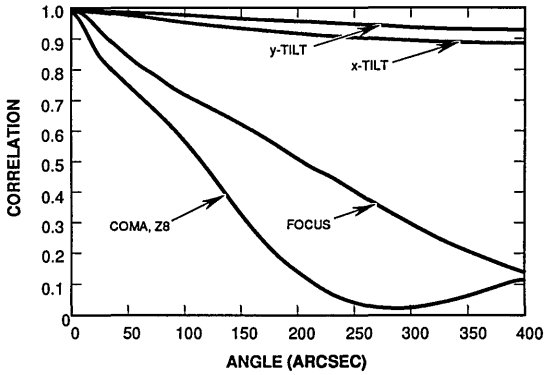

(a)

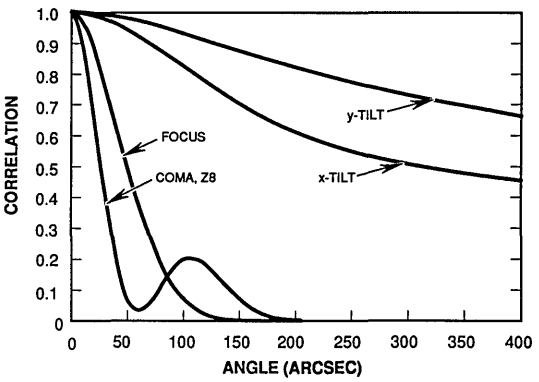

(b)

Fig. 15. Correlation parameter Γ_n of Eqs. (A6) and (A7) for Zernike modes over an 8-m aperture as a function of off-axis field-star angle, for (a) MK turbulence and (b) MMK turbulence. The correlation parameters for the tilt, the focus, and the coma at $\lambda = 0.5$ μm, $\lambda = 1.0$ μm, and $\lambda = 2.0$ μm are shown.

$$\sigma_\theta{}^{\text{noise}} = \frac{\lambda/D}{4\text{SNR}\int_0^1 H(xD,0)\mathrm{d}x}, \tag{A12}$$

where H is the optical transfer function[38] of the imaging system. The factor SNR is the signal-to-noise ratio:

$$\text{SNR} = \frac{N}{(4n^2 + N)^{1/2}}, \tag{A13}$$

where N is the number of detected photons and n is the rms readout noise per pixel from the sky background and the detector. For a point source that is imaged through Kolmogorov turbulence with a circular lens of diameter D,

$$H(xD,0) = \frac{2}{\pi}\exp\left[-3.44\left(\frac{xD}{r_0}\right)^{5/3}(1 - x^{1/3})\right] \times [\cos^{-1}(x) - x(1 - x^2)^{1/2}]. \tag{A14}$$

The numerical evaluation of Eqs. (A12) and (A14) results in Eq. (26) for the rms centroid error, which we repeat here:

$$\sigma_\theta{}^{\text{noise}} = \alpha w \frac{\lambda}{D}\frac{1}{\sqrt{N}}\left(1 + \frac{4n^2}{N}\right)^{1/2}. \tag{A15}$$

In Eq. (A15), w is the FWHM of the image in units of the diffraction-limited image width λ/D, and the parameter α depends on D/r_0. For $D/r_0 = 1$ through $D/r_0 = 8$, ranging from diffraction limited to uncorrected images, α varies from 1.1 to 0.6. For the cases considered in Section 5, $\alpha \cong 0.7$.

APPENDIX 3: PISTON RECONSTRUCTION ALGORITHM

The Shack–Hartmann measurements correspond to edge-to-edge slope values across the subapertures, as is pictured in Fig. 12. The phase difference in the x direction across subaperture ij with midpoint $\mathbf{r}_{ij}$ is

$$\Delta\phi_{ij}{}^x = \frac{4}{\pi\mathrm{d}}\int w_{ij}(\mathbf{r})\nabla_x\Phi(\mathbf{r})\mathrm{d}\mathbf{r} + n_{ij}, \tag{A16}$$

where $w_{ij}(\mathbf{r}) = w(\mathbf{r} - \mathbf{r}_{ij})$ is a window on the subaperture and n_{ij} is the measurement noise (assumed to be white noise) with variance $\sigma_{\text{pd}}{}^2$. The phase difference $\Delta\phi_{ij}{}^x$ is equal to $ds_{ij}{}^x$, where $s_{ij}{}^x$ is the x slope across the subaperture. The least-squares reconstruction algorithm as implemented for the telescope will derive the 52 pistons from the 104 phase-difference measurements with an optimal algorithm that takes into account the finite detector area and Kolmogorov statistics and employs a noise filter. (For examples of optimal phase reconstruction, see Ref. 39.) For the purpose of studying different geometries and SNR's, however, we have treated the traditional case of discrete points, as is shown in Fig. 12. In this approximation the slopes are related to the desired phases by

$$\Phi_{i+1,j} - \Phi_{ij} = \frac{d}{2}(s_{i+1,j}{}^x + s_{ij}{}^x). \tag{A17}$$

To determine the Φ_{ij} we minimize the quantity

$$\sum_{ij}\left[\hat{\Phi}_{i+1,j} - \hat{\Phi}_{ij} - \frac{d}{2}(s_{i+1,j}{}^x + s_{ij}{}^x)\right]^2 + \left[\hat{\Phi}_{i,j+1} - \hat{\Phi}_{ij} - \frac{d}{2}(s_{i,j+1}{}^y + s_{ij}{}^y)\right]^2 \tag{A18}$$

with respect to an arbitrary phase element $\hat{\Phi}_{kl}$. This results in a Poisson differential equation

$$\nabla^2\hat{\Phi}_{ij} = \nabla\cdot\mathbf{s}_{ij}, \tag{A19}$$

where the Laplacian and the divergence operators correspond to finite-difference operations among grid points. Equation (A19) can be solved with matrix inversion, although a zero-mean constraint[40] on the output phases is required because of the invariance of the measurements with respect to the addition of an arbitrary overall piston. For our simulations, however, we used the iterative successive overrelaxation algorithm that is described in Ref. 31, which is useful for exploring different cases quickly, since a new inverse does not have to be computed each time.

The successive overrelaxation algorithm updates the phases at time t, $\hat{\Phi}_{ij}(t)$, by means of

$$\hat{\Phi}_{ij}(t+1) = \hat{\Phi}_{ij}(t) + \omega[\overline{\Phi}_{ij}(t) + b_{ij}/g_{ij} - \hat{\Phi}_{ij}(t)], \tag{A20}$$

where

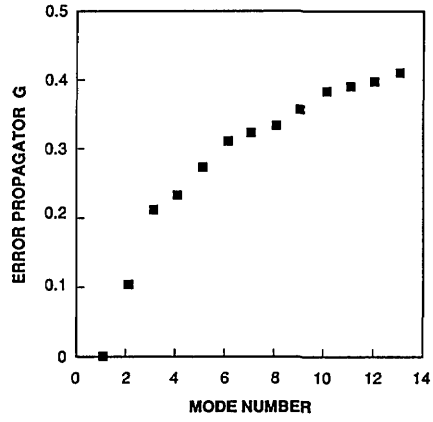

Fig. 16. Value of the noise propagator G, given in Eq. (29), for phase reconsruction over the subaperture arrangement that is shown in Fig. 12, as a function of increasing Zernike-mode index.

$$\overline{\Phi}_{ij}(t) = [\hat{\Phi}_{i+1,j}(t) + \hat{\Phi}_{i-1,j}(t) + \hat{\Phi}_{i,j+1}(t) + \hat{\Phi}_{i,j-1}(t)], \quad \text{(A21)}$$

$$b_{ij} = (s_{i-1,j}{}^{x} - s_{ij}{}^{x} + s_{i,j-1}{}^{y} - s_{ij}{}^{y}), \quad \text{(A22)}$$

$$g_{ij} = 2, \quad i = 1 \text{ or } n_i, j = 1 \text{ or } n_j,$$

$$= 3\begin{cases} i = 1 \text{ or } n_i, & j = 2 \text{ to } n_j - 1, \\ i = 2 \text{ to } n_i - 1, & j = 1 \text{ or } n_j \end{cases},$$

$$= 4 \quad \text{otherwise}. \quad \text{(A23)}$$

In Eq. (A23), n_i is the last subaperture in row n_i, and n_j is the last subaperture in column j. In Eq. (A20), ω is a relaxation parameter, $1 \le \omega \le 2$.

The reconstruction error is defined as

$$\sigma_{\phi}{}^{\text{rec}} = \left[\frac{1}{N}\sum_{ij}\langle(\hat{\Phi}_{ij} - \Phi_{ij})^2\rangle\right]^{1/2}. \quad \text{(A24)}$$

The mean-square reconstruction error can be expressed in units of noise variance:

$$(\sigma_{\phi}{}^{\text{rec}})^2 = G\sigma_{\text{pd}}{}^2. \quad \text{(A19)}$$

In Eq. (A25), G is the noise propagator or gain. It is well known[31,40] that solutions to Eq. (A19) have propagators that are less than unity for small- to moderate-sized grids. In our case, by performing reconstructions of simulated data and by calculating the error with Eq. (A24), we find that $G = 0.5$. The noise propagation can be analyzed in terms of Zernike modes to show how accurately the slopes integrate for varying scale sizes. Figure 16 shows the increase in G as Zernike modes are successively added. To calculate the value of G for a given mode m, subtract the value shown for that mode from the value for the previous mode $m - 1$. From the figure we can see that slope reconstruction results in considerable smoothing, since only ~20% of the reconstruction error is in the highest spatial frequencies. Approximately 60% of the error is in tilt (which can be removed), focus, and astigmatism. This result has implications for dim natural sources, where σ_{pd} could become an appreciable fraction of a wave. However, in Section 6 we showed that this is not the case for laser stars.

ACKNOWLEDGMENTS

We thank N. J. Woolf for a critical reading of the manuscript and many useful conversations. Steward Observatory acknowledges support from the National Science Foundation and the Flintridge Foundation. ThermoTrex thanks Dwight Duston of the Ballistic Missile Defense Organization, Innovative Science and Technology, Bob Mongeon and Matt White of the U.S. Office of Naval Research, and Vern Smiley of U.S. Navy Research and Development for supporting research in defense applications of laser-guide-star adaptive optics, on which much of this research was based.

D. G. Sandler is also with the Steward Observatory.

REFERENCES

1. H. W. Babcock, "The possibility of compensating astronomical seeing," Publ. Astron. Soc. Pac. **65,** 229–236 (1953).
2. J. C. Fontanella, G. Rousset, and P. Lena, "Adaptive optics, a key element of the VLT," J. Opt. (Paris) **22,** 99–101 (1991).
3. F. Roddier, M. Northcott, and J. E. Graves, "A simple low-order adaptive optics system for near-infrared applications," Publ. Astron. Soc. Pac. **103,** 131–149 (1991).
4. J. E. Graves, D. L. McKenna, M. J. Northcott, and F. Roddier, "The UH prototype adaptive optics system," in *Adaptive Optics for Large Telescopes*, Vol. 19 of 1992 OSA Technical Digest Series (Optical Society of America, Washington, D.C., 1992), pp. 173–175.
5. M. Lloyd-Hart, R. Dekany, B. McLeod, D. Wittman, D. Colucci, D. McCarthy, and R. Angel, "Direct 75 milliarcsecond images from the Multiple Mirror Telescope with adaptive optics," Astrophys. Lett. **402,** L81–L84 (1993).
6. R. Q. Fugate, D. L. Fried, G. A. Ameer, B. R. Boeke, S. L. Browne, P. H. Roberts, R. E. Ruane, G. A. Tyler, and L. M. Wopat, "Measurements of atmospheric wavefront distortion using scattered light from a laser guide star," Nature (London) **353,** 144–146 (1991).
7. C. A. Primmerman, D. V. Murphy, D. A. Page, G. Zollars, and H. T. Barclay, "Compensation of atmospheric optical distortion using a synthetic beacon," Nature (London) **353,** 141–143 (1991).
8. D. G. Sandler, L. Cuellar, M. Lefebvre, T. Barrett, R. Arnold, P. Johnson, A. Rego, G. Smith, G. Taylor, and B. Spivey, "Shearing interferometry for laser-guide-star atmospheric correction at large D/r_0," J. Opt. Soc. Am. A **11,** 858–873 (1994).
9. P. Strittmatter, "Columbus Project Telescope," in *Advanced Technology Optical Telescopes IV*, L. D. Barr, ed., Proc. Soc. Photo-Opt. Instrum. Eng. **1236,** 71–78 (1990).
10. E. Kibblewhite, "Laser beacons for astronomy," presented at the Workshop on Laser Guide Star Adaptive Optics, Albuquerque, N.M., 1992.
11. C. S. Gardner, B. M. Welsh, and L. A. Thompson, "Design and performance analysis of adaptive optical telescopes using laser guide stars," Proc. IEEE **78,** 1721–1743 (1990).
12. R. Thompson, M. Rieke, E. Young, D. McCarthy, R. Rasche, M. Blessinger, K. Vural, and W. Kleinhaus, "Future directions for NICMOS arrays," in *Proceedings of Third Infrared Detector Technology Workshop*, C. R. McCreight, ed., NASA Tech. Memo 102209 (NASA, Washington, D.C., 1989).
13. D. Wittman, J. R. P. Angel, M. Lloyd-Hart, D. Collucci, and D. McCarthy, "Optical sensing of infrared wavefronts for adaptive control: a new CCD detector and MMT experiments," in Vol. 42 of *Proceedings of European Southern Observatory Conference on Progress in Telescope and Instrumentation Technologies*, M.-H. Ulrich, ed. (European Southern Observatory, Garching, Germany, 1992), pp. 453–460.
14. J. C. Geary "Rapid-framing low-noise CCD imagers for adaptive optics," presented at the Workshop on Laser Guide Star Adaptive Optics, Albuquerque, N.M., 1992.
15. M. P. Lesser, A. Bauer, L. Ulrickson, and D. Ouellette, "Bump bonded back illuminated CCDs," in *High-Resolution*

Sensors and Hybrid Systems, M. M. Blouke, W. Chang, R. P. Khoslan, and L. J. Thorpe, eds., Proc. Soc. Photo-Opt. Instrum. Eng. **1656,** 508–516 (1992).
16. V. I. Tatarski, *Wave Propagation in a Turbulent Medium* (Dover, New York, 1961).
17. D. L. Fried, "Optical resolution through a randomly inhomogeneous medium for very long and very short exposures," J. Opt. Soc. Am. **56,** 1372–1379 (1966).
18. R. J. Noll, "Zernike polynomials and atmospheric turbulence," J. Opt. Soc. Am. **66,** 207–211 (1976).
19. D. L. Fried, "Anisoplanatism in adaptive optics," J. Opt. Soc. Am. **72,** 52–61 (1982).
20. D. P. Greenwood and D. L. Fried, "Power spectra requirements for wave-front compensative systems," J. Opt. Soc. Am. **66,** 193–206 (1976).
21. F. Roddier, L. Cowie, J. E. Graves, S. Songaila, D. McKenna, J. Vernin, M. Azount, J. L. Caccia, E. Limburg, C. Roddier, D. Salmon, S. Beland, D. Cowley, S. Hill, "Seeing at Mauna Kea: a joint UH-UN-NOAO-CFHT study," in *Advanced Technology Optical Telescope IV*, L. D. Barr, ed., Proc. Soc. Photo-Opt. Instrum. Eng. **1236,** Part 1, 485–491 (1990).
22. R. R. Beland, "A decade of balloon microthermal probe measurements of optical turbulence," in *Adaptive Optics for Large Telescopes*, Vol. 19 of 1992 OSA Technical Digest Series (Optical Society of America, Washington, D.C., 1992), pp. 14–16.
23. G. C. Valley and S. M. Wandzura, "Spatial correlation of phase-expansion coefficients for propagation through atmospheric turbulence," J. Opt. Soc. Am. **69,** 712–717 (1979).
24. G. A. Tyler, "Bandwidth considerations for tracking through turbulence," Rep. TR-887 (Optical Sciences Company, Placentia, Calif., 1988).
25. G. A. Tyler, "Turbulence-induced adaptive-optics performance degradation: evaluation in the time domain," J. Opt. Soc. Am. A **1,** 251–262 (1984).
26. J. R. P. Angel, "Use of natural stars with laser beacons for large telescope adaptive optics," presented at the Workshop on Laser Guide Star Adaptive Optics, Albuquerque, N.M., (1992).
27. J. N. Bahcall and R. M. Soniera, "Predicated star counts in selected fields and photometric bands: applications to galactic structure, the disk luminosity function, and the detection of a massive halo," Astrophys. J. Suppl. Ser. **47,** 357–401 (1981).
28. R. J. Wainscoat, M. Cohen, K. Volk, H. J. Walker, and D. E. Schwartz, "A model of the 8–25 μm point source infrared sky," Astrophys. J. Suppl. Ser. **83,** 111–146 (1992).
29. D. L. Fried, "Analysis of focus anisoplanatism: the fundamental limit in performance of artificial guide star adaptive optics systems," presented at the Workshop on Laser Guide Star Adaptive Optics, Albuquerque, N.M., 1992.
30. D. Sandler, "A multiple spot laser beacon for high-order wavefront control: theory and experiment," presented at the Workshop on Laser Guide Star Adaptive Optics, Albuquerque, N.M., 1992.
31. W. H. Southwell, "Wave-front estimation from wave-front slope measurements," J. Opt. Soc. Am. **70,** 998–1006 (1980).
32. M. P. Jelonek, R. Q. Fugate, W. J. Lange, A. L. Slavin, R. E. Ruane, R. A. Cleis, "Sodium laser guide star experiments at Starfire Optical Range," presented at the Workshop on Laser Guide Star Adaptive Optics, Albuquerque, N.M., 1992.
33. T. H. Jeys, "Mesopheric laser beacon," presented at the Workshop on Laser Guide Star Adaptive Optics, Albuquerque, N.M., 1992.
34. H. Friedman, J. Morris, and J. Horton, "System design for high power sodium beacon laser," presented at the Workshop on Laser Guide Star Adaptive Optics, Albuquerque, N.M., 1992.
35. B. Ellerbroek, "Fitting error coefficients for three segmented mirror–Hartmann sensor configurations," Rep. RDA-TR23-1502 (R&D Associates, Albuquerque, N.M., 1991).
36. G. A. Tyler, "Analysis of propagation through turbulence: evaluation of an integral involving the product of three Bessel functions," J. Opt. Soc. Am. A **7,** 1218–1223 (1990).
37. G. Tyler and D. L. Fried, "Image position error associated with a quadrant detector," J. Opt. Soc. Am. **72,** 804–808 (1982).
38. J. W. Goodman, *Statistical Optics* (Wiley, New York, 1985).
39. E. P. Walner, "Optimal wavefront correction using slopes measurements," J. Opt. Soc. Am. **73,** 1771–1776 (1983).
40. J. Hermann, "Least-squares wavefront errors of minimum norm," J. Opt. Soc. Am. **70,** 28–33 (1980).